J. Fluid Mech. (1995), *vol.* 284, *pp.* 275–321

Asymptotic vorticity structure and numerical simulation of slender vortex filaments

By RUPERT KLEIN[1] AND OMAR M. KNIO[2]

[1] Institut für Technische Mechanik, RWTH, Templergraben 64, 52056 Aachen, Germany

[2] Department of Mechanical Engineering, The Johns Hopkins University, Baltimore, MD 21218, USA

(Received 3 June 1994 and in revised form 6 September 1994)

A new asymptotic analysis of slender vortices in three dimensions, based solely on the vorticity transport equation and the non-local vorticity–velocity relation gives new insight into the structure of slender vortex filaments. The approach is quite different from earlier analyses using matched asymptotic solutions for the velocity field and it yields additional information. This insight is used to derive three different modifications of the thin-tube version of a numerical vortex element method. Our modifications remove an $O(1)$ error from the node velocities of the standard thin-tube model and allow us to properly account for any prescribed physical vortex core structure independent of the numerical vorticity smoothing function. We demonstrate the performance of the improved models by comparison with asymptotic solutions for slender vortex rings and for perturbed slender vortex filaments in the Klein–Majda regime, in which the filament geometry is characterized by small-amplitude–short-wavelength displacements from a straight line. These comparisons represent a stringent mutual test for both the proposed modified thin-tube schemes and for the Klein–Majda theory. Importantly, we find a convincing agreement of numerical and asymptotic predictions for values of the Klein–Majda expansion parameter ϵ as large as $\frac{1}{2}$. Thus, our results support their findings in earlier publications for realistic physical vortex core sizes.

1. Introduction

A slender vortex flow as sketched in figure 1 is characterized by a vorticity distribution that is highly concentrated in the vicinity of a smooth time-dependent curve $L(t)$: $s \to X(s, t)$. A typical diameter d of the vortex core is small compared to a characteristic radius of curvature R of $L(t)$. Thus the dimensionless parameter $\delta = d/R$ satisfies

$$\delta = d/R \ll 1. \tag{1.1}$$

An important application for the theory of slender vortices is the prediction of the behaviour of the trailing vortices behind aircraft wings (Crow 1970; Ting 1971; Widnall 1975 and references therein). Chorin (1982) and Chorin & Akao (1991) suggest that slender vortices play an important role in governing the structure of turbulent flows, and Pumir & Siggia (1990) propose that the interaction of slender vortices may lead to the collapse of solutions to the fluid equations. In addition, slender vortices represent a class of flow fields that allows one to study fundamental aspects of fluid mechanics such as vortex (self-) stretching and the often-cited energy transfer in wavenumber space in a specialized framework (Klein & Majda 1991*a*, *b*, 1993; Klein,

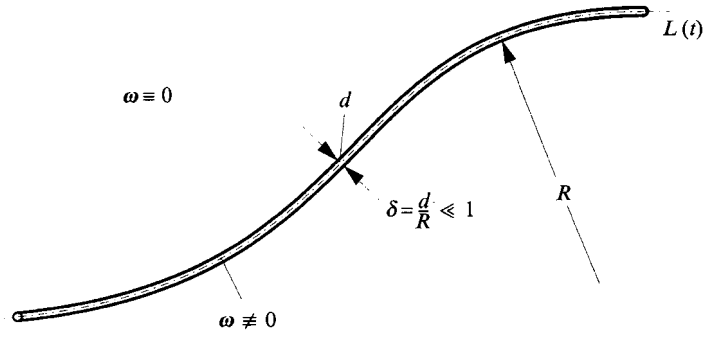

FIGURE 1. Section of a slender vortex with the vorticity concentrated in a thin tube of characteristic diameter d centred around a smooth time-dependent curve $L(t)$ with characteristic radius of curvature $R \gg d$.

Majda & McLaughlin, 1992). Thus, there is ample motivation for studies of the dynamics of slender vortex filaments.

Early, more or less heuristic attempts at deriving suitable evolution equations for slender vortices in three space dimensions involved the *local induction approximation*, which is based on neglecting all non-local effects of vortex self-induction (Arms & Hama 1965). Systematic analyses using methods of matched asymptotic expansions revealed the precise mathematical form of the non-local induction terms in the filament equation of motion (Ting 1971; Callegari & Ting 1978) and the extended asymptotic and numerical studies by Klein & Majda (1991*a*, *b*) showed their significance in generating several well-known fluid-mechanical phenomena. The search for reliable predictions of vortex filament dynamics also included studies based on numerical techniques. The review article by Leonard (1985) summarizes several earlier approaches and we mention in addition the work by Liu, Tavantsis & Ting (1986) who implemented numerically the system of equations derived through systematic asymptotic analyses by Callegari & Ting (1978) and the thin-tube model approach used by Knio & Ghoniem (1990), which is the basis for the numerical methods discussed in the present work.

Detailed asymptotic analyses, e.g. by Callegari & Ting (1978), Ting & Klein (1991) or Klein & Majda (1991*a*) and the present derivations in §2 of this paper, show that under certain conditions of quasi-steadiness the reference line $L(t)$ of a slender vortex moves in space according to the propagation law

$$\boldsymbol{X}_t = \frac{\Gamma}{4\pi}(\ln(2/\delta) + C)\,\kappa\boldsymbol{b} + \boldsymbol{Q}^f(\boldsymbol{X}). \tag{1.2}$$

Here Γ is the overall circulation of the vortex, κ and $\boldsymbol{b}$ are the local curvature and unit binormal vector at $\boldsymbol{X}$ on $L(t)$, respectively. The quantity C is a core structure coefficient defined by

$$C = \lim_{r\to\infty}\left(\frac{4\pi^2}{\Gamma^2}\int_0^{\bar{r}} r' v^{(0)^2}\,\mathrm{d}r' - \ln r'\right) - \tfrac{1}{2} - \frac{8\pi^2}{\Gamma^2}\int_0^{\infty} r' w^{(0)^2}\,\mathrm{d}r', \tag{1.3}$$

where $v^{(0)}(\bar{r}, t)$, $w^{(0)}(\bar{r}, t)$ are the leading-order axisymmetric axial and circumferential velocities in the vortex core and $\bar{r} = r/\delta$ is a stretched radial coordinate in the planes normal to $L(t)$. The last contribution $\boldsymbol{Q}^f$ in (1.2) is the so-called finite part of the line Biot–Savart integral which represents the influence of non-local self-induction of the vortex. We provide a precise definition of $\boldsymbol{Q}^f$ in §2.

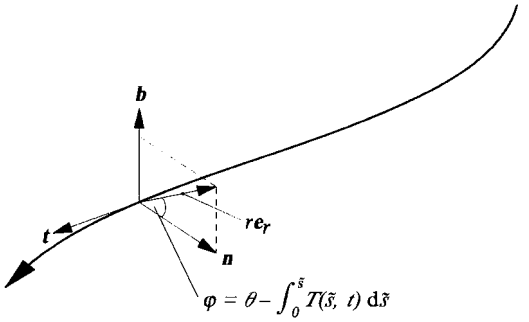

FIGURE 2. Filament-attached coordinates following Callegari & Ting (1978).

The formulae in (1.2) and (1.3) reveal the major difficulties associated with the mathematical description of slender vortices.

(i) The leading term in δ in (1.2) is of order $(\Gamma/R)\ln(1/\delta)$, which is about one order of magnitude smaller than the maximum circumferential velocities in the vortical core. The latter are of $O(\Gamma/d) = O((1/\delta)(\Gamma/R))$, in accordance with the scaling behaviour of a potential vortex. Thus, the net motion of the filament in space is the result of a subtle cancellation of much larger velocities in the core. This feature results in a stiff nature of the governing equations in the small-δ limit.

(ii) The second term in (1.2) involves the local core structure coefficient, C, from (1.3). This term is as large, namely of $O(1)$, as the non-local contribution $\boldsymbol{Q}^I$ and should therefore not be neglected. Keeping this term, however, requires an accurate representation of the vortex core structure, or at least of the integral quantity C, and makes an *ad hoc* approximation of the local induction effects unacceptable.

(iii) The finite part of the line Biot–Savart integral $\boldsymbol{Q}^I$ in (1.2) is a complex non-local and nonlinear expression that involves the principal value of a singular integral. The numerical evaluation of such an expression is a stiff procedure and should be avoided if possible.

One of the goals of this paper is to develop a suitable modification of the thin-tube version of a general vortex element solver which (*a*) removes part of the stiffness associated with (i) above, (*b*) allows us to accurately represent the influence of the vortex core structure on the filament motion including a non-trivial axial flow, and (*c*) yields an asymptotically correct representation of the non-local induction effects. The idea is to first perform a detailed asymptotic analysis of slender vortex solutions of the fluid equations in the vorticity–velocity formulation and then to implement the knowledge gained in the thin-tube version of a numerical vortex element scheme. In the next paragraphs we first explain our new asymptotic approach and then summarize the design of the numerical method and of its asymptotics-induced modifications.

Summary of the asymptotic analysis

In §§2 and 3 we analyse the vorticity transport equation for inviscid flow:

$$\omega_t + (v\cdot\nabla)\omega = (\omega\cdot\nabla)v, \tag{1.4}$$

and the nonlinear–nonlocal velocity–vorticity relation:

$$v(X,t) = \frac{1}{4\pi}\iiint \frac{x'-X}{|x'-X|^3}\times\omega(x',t)\,\mathrm{d}^3x', \tag{1.5}$$

which we call the three-dimensional Biot–Savart integral henceforth. We consider

special solutions of (1.4), (1.5) with the following asymptotic structure. We let $\delta \ll 1$ from (1.1) be a small expansion parameter, $L(t)\colon s \to \boldsymbol{X}(s,t)$ the time-dependent filament reference curve and r, θ, s the filament-attached coordinate system as sketched in figure 2 (see also Callegari & Ting 1978). Each plane normal to the reference curve at $\boldsymbol{X}(s,t)$, say, is spanned by cylindrical coordinates r, θ. Here θ is a circumferential angle with the line $\theta = 0$ in each normal plane chosen such that at all times (r, θ, s) are orthogonal (see also §3). Then we consider flow fields with vorticity distributions concentrated in the vicinity of $L(t)$, so that

$$\begin{aligned}\boldsymbol{\omega}(\boldsymbol{x}, t; \delta) = {} & \frac{1}{\delta^2}(\eta^{(0)}(r/\delta, s, t)\,\boldsymbol{e}_\theta + \zeta^{(0)}(r/\delta, s, t)\,\boldsymbol{t}) \\ & + \frac{1}{\delta}(\xi^{(1)}(r/\delta, \theta, s, t)\,\boldsymbol{e}_r + \eta^{(1)}(r/\delta, \theta, s, t)\,\boldsymbol{e}_\theta + \zeta^{(1)}(r/\delta, \theta, s, t)\,\boldsymbol{t}) \\ & + O(1). \end{aligned} \tag{1.6}$$

Here $\xi^{(i)}$, $\eta^{(i)}$, $\zeta^{(i)}$ are asymptotic expansion functions for the radial, circumferential and axial vorticity components in the vortex core, respectively, and $\boldsymbol{e}_r$, $\boldsymbol{e}_\theta$, $\boldsymbol{t}$ are the mutually orthogonal radial, circumferential and axial unit vectors. Notice that $\eta^{(0)}(\bar{r}, s, t)$, $\zeta^{(0)}(\bar{r}, s, t)$, with $\bar{r} = r/\delta$, are assumed not to depend on θ, so that the leading-order core structure is axisymmetric. Furthermore in (1.6), time is normalized by the reference time

$$t_{ref} = 4\pi R^2/\Gamma, \tag{1.7}$$

which is larger by two orders of magnitude than the characteristic turnover time of the vortex core, $t_{core} = 4\pi d^2/\Gamma$. Thus, we assume a smooth evolution of the filament geometry and an associated quasi-steady behaviour of the vortex core.

The general task of an asymptotic analysis is then to derive (*a*) an equation of motion for $L(t)$ in terms of the leading-order core structure and the instantaneous curve geometry, and (*b*) associated evolution equations for the leading-order core structure. Here we concentrate on the first part, the equation of motion for $L(t)$, because the results of this analysis will be crucial in deriving the desired improvement of the thin-tube numerical scheme. That is, in this paper we consider the leading-order core structure to be given and we provide an accurate description of the filament motion under that premise. In fact, in all explicit examples of §5, the core structure is asymptotically constant on the timescales considered (see Klein & Majda 1991*a*), consistent with the Euler equations. More general situations with vortex stretching and viscous diffusion playing a non-trivial role will be considered in the near future (see Klein, Ting & Knio 1994).

We insert the ansatz (1.6) into the three-dimensional Biot–Savart integral and obtain a general asymptotic expression for the induced velocities on $L(t)$ in (1.2). At this stage of the calculation, the core coefficient C is expressed in terms of the leading- and first-order axial vorticities as

$$C = -\left(\frac{1}{2} + \frac{2\pi}{\Gamma}\int_0^\infty \left[\frac{1}{\kappa}\zeta_{11}^{(1)} + \bar{r}\ln\bar{r}\,\zeta^{(0)}\right]\mathrm{d}\bar{r}\right). \tag{1.8}$$

Here $\zeta_{11}^{(1)}(\bar{r}, t)$ is the first cosine Fourier mode with respect to θ of the first-order axial vorticity, defined by the relation

$$\zeta^{(1)} = \sum_j \zeta_{j1}^{(1)}\cos(j\theta) + \zeta_{j2}^{(1)}\sin(j\theta). \tag{1.9}$$

Two observations regarding (1.2) in connection with (1.8) have led us to the modified thin-tube vortex element schemes proposed in this paper. Let $\tilde{L}(t)$ be a space

curve that is displaced from the filament reference line $L(t)$ by a distance of $O(\delta^2)$. Then one finds that:

(i) The formulae (1.2) and (1.8) also yield the induced velocities on $\tilde{L}(t)$, provided that a representation $\tilde{\zeta}_{11}^{(1)}(\bar{r}, t)$ for the contribution of the first-order vorticity is introduced which is valid in the coordinate frame attached to $\tilde{L}(t)$. The difference between $\zeta_{11}^{(1)}$ and $\tilde{\zeta}_{11}^{(1)}$ simply corresponds to an $O(\delta^2)$ spatial displacement of the leading-order axisymmetric core structure.

(ii) The induced velocities at points on $L(t)$ and $\tilde{L}(t)$ differ by $O(1)$ due to this difference between $\zeta_{11}^{(1)}$ and $\tilde{\zeta}_{11}^{(1)}$ or, equivalently, they differ due to the large velocity gradient of $O(\delta^{-2})$ in the core.

In § 3 we use the fact that there must be a particular curve $L^{st}(t)$ in an inner $O(\delta^2)$ core of the filament on which the induced velocity coincides with the speed of points on $L(t)$ except for an irrelevant axial velocity component. We call $L^{st}(t)$ the connecting line of local stagnation points in the moving frame of reference and show that the core coefficient C associated with $L^{st}(t)$ has the representation announced in (1.3).

Improvement of the thin-tube model (ttm)

Various techniques for the numerical simulation of vortex dynamics have been proposed in the literature, e.g. by Chorin (1980), Beale & Majda (1985) or Knio & Ghoniem (1990). Here we concentrate on the *thin-tube* vortex element scheme (*ttm*) proposed by Knio & Ghoniem which is a simplified version of Beale & Majda's well-analysed general vortex element method for three-dimensional incompressible flows. The scheme represents a slender vortex by a single chain of overlapping vortex elements. The elements are characterized by a common circulation Γ, by the time-dependent end points of associated filament line segments $\{\boldsymbol{\chi}_i(t)\}_{i=1}^{N}$ and by a prescribed spherically symmetric and rapidly decaying vorticity smoothing function $f_{\delta^{ttm}}$. Here δ^{ttm} is a numerical core size parameter whose relation to the physical slender vortex core structure remains to be established. At any given time, the vorticity distribution of the slender vortex is approximated by

$$\boldsymbol{\omega}(\boldsymbol{x}, t) = \Gamma \sum_{i=1}^{N} (\boldsymbol{\chi}_{i+1} - \boldsymbol{\chi}_i)(t) f_{\delta^{ttm}}\left(\boldsymbol{x} - \frac{\boldsymbol{\chi}_{i+1} + \boldsymbol{\chi}_i}{2}(t)\right). \tag{1.10}$$

This distribution is evolved in time by moving the nodes $\boldsymbol{\chi}_i(t)$ in a Lagrangian fashion. Thus, to advance the solution in time, one integrates the ordinary differential equations:

$$\frac{\mathrm{d}\boldsymbol{\chi}_i}{\mathrm{d}t} = \boldsymbol{v}_i^*, \tag{1.11}$$

where $\boldsymbol{v}_i^*$ is the velocity at $\boldsymbol{\chi}_i$ induced by the vorticity distribution (1.10). In this fashion, the approximate filament geometry is updated from one time step to the next.

One key advantage of the underlying vortex element method that is inherited by the simplified thin-tube model is the numerically exact integration of the three-dimensional Biot–Savart integral (1.5) for the nodes $\boldsymbol{\chi}_i(t)$, given the vorticity distribution in (1.10). Observing that the non-local finite part $\boldsymbol{Q}^f$ of the line Biot–Savart integral in (1.2) would be the same for all the points in a given cross-section of the vortex core, we notice that the evaluation of (1.5) at the nodes will incorporate automatically a highly accurate approximation for $\boldsymbol{Q}^f$. Only the local induction effects need to be analysed in more detail.

There is a close relationship between this numerical method for vortex filament computations and the asymptotic theory discussed in the previous paragraphs. Both theories are based on the vorticity–velocity formulation for inviscid flows, assume a

quasi-steady vortex core structure and rely on a suitable evaluation of the Biot–Savart integral in order to arrive at an expression for the local velocity of points on the filament reference line. We will explore this conceptual similarity in this paper in order to (i) reveal and remedy the deficiencies of the numerical method using new insight from an asymptotic limit consideration and (ii) to assess the regime of applicability of the asymptotics.

In §4 we present a detailed asymptotic analysis of the thin-tube vortex element scheme. By comparing the numerical vortex core structure with the asymptotic predictions from §§2 and 3 we find that the vortex element nodes lie on a curve $L^{ttm}(t)$ that differs from the connecting line of stagnation points $L^{st}(t)$ by an $O(\delta^2)$ distance. Argument (ii) above then implies that the computed induced velocities at the nodes are not the desired filament velocities. In fact, an $O(1)$ velocity error occurs due to a false (or 'inconsistent') representation of the *local induction*. This error can be corrected in various ways, three of which we discuss and test in this work. The first is an explicit additive correction of the induced velocities at the vortex element nodes. The second relies on evaluating the induced velocities not at the vortex element nodes but on those points on $L^{st}(t)$ that are closest to the nodes. For the second method we derive and implement asymptotic expressions for the node-to-stagnation point distance. Finally, a third correction method is derived which is based on an appropriate rescaling of the numerical core size parameter δ^{ttm} so that local induction effects are properly accounted for.

We emphasize again that in the present paper we concentrate on a regime where the leading-order vortex core structure would not change appreciably on the timescales considered, so that it is identical to the initial core vorticity distribution. The latter can be assumed given through a suitable choice of the initial data for the flow. An extension to regimes with non-trivial evolution of the vortex cores due to vortex stretching and viscous diffusion is currently being developed (Klein *et al.* 1994).

The comparison of numerical predictions and asymptotic analysis

Section 5 contains detailed comparisons of the standard and corrected thin-tube models with slender vortex asymptotics. We consider perturbed slender vortices in the Klein–Majda regime, which we summarize in the next paragraph and explain in more detail in §2. In §6, in the framework of a general discussion of the achievements of this work, we demonstrate the aforementioned $O(1)$ error of the standard thin-tube model by evaluating the velocity of thin vortex rings.

Klein & Majda (1991*a*, *b*) analyse a particular regime for slender vortex flows by combining and extending the matched asymptotic analysis of Callegari & Ting (1978) and Hasimoto's transformation (Hasimoto 1972). The resulting theory yields an improved understanding of the effects of nonlinear–non-local interactions on the dynamics of perturbed slender vortices. Slender vortices in the Klein–Majda regime are characterized by small-amplitude geometric perturbations that are superimposed on otherwise straight filaments. In this regime the amplitudes and wavelengths of these displacements are assumed to be large compared to the vortex core size, but still small compared to a typical radius of curvature of the filament reference line. Specifically, when $\epsilon = \lambda/R$ is the ratio of a typical perturbation wavelength to the characteristic radius of curvature of the filament, then the displacement amplitudes are of order $\epsilon^2 R$, and ϵ is related to the core size parameter δ through the distinguished limit

$$\epsilon^2 = \frac{2}{\ln(2\epsilon/\delta) + C}. \tag{1.12}$$

Klein & Majda (1991*a*) show that this relation guarantees non-trivial interactions of nonlinear curvature effects with the non-locality from the finite part of the Biot–Savart integral for which a linearized expression, valid in the limit of $\epsilon \to 0$, is given.

The comparison of modified thin-tube vortex element predictions with the Klein–Majda asymptotics represents a stringent mutual test for these two very different approaches. We first present static comparisons of the predicted filament velocities based on prescribed geometries, which later serve as initial data for dynamical computations. An important aspect of these comparisons concerns the range of vortex core sizes that we choose and the ranges of applicability of the numerics and asymptotics. The slender vortex asymptotics is designed for the limit of small core sizes so that its reliability improves as δ diminishes. On the other hand, vortex element thin-tube model computations become unaffordable owing to increasing resolution and time step requirements as the core size decreases. In our example calculations of § 5, we choose core sizes for which the expansion parameter ϵ from (1.12) is as large as $\frac{1}{2}$. Nevertheless, we achieve quite a convincing agreement between the asymptotic and numerical predictions. Thus, with the slender vortex asymptotics one has another example where asymptotic predictions yield unexpectedly accurate results at the formal border of their regime of applicability.

2. Basic considerations

2.1. *Formulation*

As previously mentioned, two modelling approaches are adopted in this paper to analyse the motion of slender vortex filaments. In the first approach, matched asymptotic expansions are used to reduce the governing equations to a simplified 'filament equation' for a scalar complex function ψ that contains all the geometrical information of the filament reference line. The second approach is a three-dimensional simulation based on a vortex element method.

Our new derivation of the asymptotic filament equations starts with the three-dimensional momentum equations in vorticity–velocity formulation:

$$\frac{\partial \boldsymbol{\omega}}{\partial t} + \boldsymbol{v} \cdot \nabla \boldsymbol{\omega} = \boldsymbol{\omega} \cdot \nabla \boldsymbol{v} + \frac{1}{Re} \nabla^2 \boldsymbol{\omega}, \tag{2.1}$$

$$\boldsymbol{v}(\boldsymbol{x}, t) = -\frac{1}{4\pi} \int \frac{(\boldsymbol{x} - \boldsymbol{y}) \times \boldsymbol{\omega}(\boldsymbol{y})}{|\boldsymbol{x} - \boldsymbol{y}|^3} \mathrm{d}\boldsymbol{y}, \tag{2.2}$$

where $\boldsymbol{v} = {}^t(u, v, w)$ is the velocity, $\boldsymbol{\omega} \equiv \nabla \times \boldsymbol{v}$ is the vorticity, t is time, and Re is the Reynolds number. The equations are normalized with respect to the reference length and velocity scales,

$$\tilde{L} = 1/\kappa_{ref}, \tag{2.3}$$

$$\tilde{V} = \Gamma \kappa_{ref}/(4\pi), \tag{2.4}$$

where κ_{ref} is a characteristic curvature of the filament reference line and Γ its circulation. We focus our attention on the high-Reynolds-number limit of the governing equations and consider filament configurations such that the core size of the filament $\delta = O(Re^{-1/2})$ is much smaller than the characteristic perturbation wavelength, which in turn is dominated by $\tilde{L}$. These assumptions enable us to use techniques of multiple scales asymptotics in order to analyse the filament dynamics (Klein 1994; Klein *et al.* 1994). We provide a summary of the key ideas, techniques and results which are of relevance to the present work in § 2.1.

Vortex filament computations are based on the *inviscid* incompressible vorticity transport equation:

$$\mathrm{D}\boldsymbol{\omega}/\mathrm{D}t = \boldsymbol{\omega}\cdot\nabla\boldsymbol{v}, \tag{2.5}$$

i.e. on (2.1) in the limit $Re\to\infty$. Here, $\mathrm{D}/\mathrm{D}t \equiv \partial/\partial t + \boldsymbol{v}\cdot\nabla$ denotes the material time derivative. Implementation of three-dimensional vortex filament schemes to model solutions of (2.5) is summarized in §4.

2.2. *The Klein–Majda regime for perturbed slender vortices*

In this section we summarize the results of the analyses by Klein & Majda (1991*a*, *b*) dealing with a special class of slender vortex flows involving at leading-order straight vortex filaments that are subjected to small-amplitude displacements. In this regime the displacements of the vortex reference lines away from the straight reference lines may be, but do not have to be, large compared to the vortex core size, but they must be small compared to a typical perturbation wavelength. In turn, the perturbation wavelengths are small compared to a characteristic filament radius of curvature. Thus, with lengths measured on the curvature scale, we consider *small-amplitude*, *short-wavelength* displacements of a slender columnar vortex. In this work, we will concentrate on the case of an isolated filament in a quiescent environment, but it should be noticed that the general theory presented in Klein & Majda (1991*a*, *b*, 1993) and Klein *et al.* (1992) allows one to also describe the dynamics of filaments embedded in a simple straining environment as well as the interaction of parallel/antiparallel pairs of slender vortices.

In §3 we will re-derive, by a new asymptotic analysis which emphasizes the vorticity structure of slender vortices, a vortex filament evolution equation with the general form

$$\boldsymbol{X}_t = \frac{1}{\epsilon^2}\kappa\boldsymbol{b} + \boldsymbol{v}, \tag{2.6}$$

with ϵ^2 defined in (1.12). The first term is the product of the filament curvature κ and the local binormal unit vector $\boldsymbol{b}$ and it corresponds to the well-known local induction approximation (see Batchelor 1967). The second term includes the effects of non-local self-induction and it is scaled in the analysis to be of order unity. The Klein–Majda regime involves slender vortex filaments whose reference lines, $L^{\epsilon}(t)$: $s\to\boldsymbol{X}(s,t;\epsilon)$, are described by

$$\boldsymbol{X}(s,t;\epsilon) = \epsilon\sigma\boldsymbol{t}_0 + \epsilon^2\boldsymbol{X}^{(2)}(\sigma,\tau) + o(\epsilon^2) \quad (\epsilon \ll 1). \tag{2.7}$$

Here we have introduced the scaled space and time coordinates

$$\sigma = s/\epsilon \quad \text{and} \quad \tau = t/\epsilon^4, \tag{2.8}$$

which appropriately resolve the characteristic length- and timescales in this regime. It has been shown that the core structure coefficient C, which enters in the ϵ–δ relationship (1.12), is constant on the characteristic time of evolution of the filament perturbations, i.e. on the timescale of τ (Klein & Majda 1991*a*).

With $\boldsymbol{t}_0$ being a constant unit vector, (2.7) is a suitable representation of small-amplitude, short-wavelength perturbations of a leading-order straight filament. Notice that $1 \gg \epsilon^2 \gg \delta$; thus, the theory accommodates displacements of the vortex which are large compared to a typical core diameter when $|\boldsymbol{X}^{(2)}| = O(1)$. However, the theory is uniformly valid in the limit $|\boldsymbol{X}^{(2)}| \ll 1$, so that the displacements do not have to be large compared to the vortex core size. In fact, Klein & Majda (1993) analyse parallel pairs of vortex filaments with the same methodology described in this section. For $|\boldsymbol{X}^{(2)}| \ll 1$

they reproduce, in a natural fashion, Crow's linear stability theory for infinitesimal perturbations of the vortex pair (Crow 1970).

When the far-field flow surrounding the filament from (2.7) is at rest, the filament motion obeys (2.6) with $\boldsymbol{v}$ given by a linearized expression for the finite part of the line Biot–Savart integral. Using the curve representation in (2.7) one finds

$$\boldsymbol{v} = \mathrm{I}[\boldsymbol{X}^{(2)}] \times \boldsymbol{t}_0. \tag{2.9}$$

The linear non-local operator $\mathrm{I}[\cdot]$, which acts on the scaled spatial variable σ, is a pseudo-differential operator

$$\mathrm{I}[w](\sigma) = \int_{-\infty}^{\infty} \frac{1}{|h|^3} [w(\sigma+h) - w(\sigma) - hw'(\sigma+h) + \tfrac{1}{2}h^2 H(1-|h|)\, w''(\sigma)]\, \mathrm{d}h, \tag{2.10}$$

whose effect is best understood by considering its Fourier symbol

$$\hat{I}(\xi) = \mathrm{e}^{-\mathrm{i}\xi\sigma}\mathrm{I}[\mathrm{e}^{\mathrm{i}\xi\sigma}] = -\xi^2(\tfrac{1}{2}\ln\xi^2 - c_0), \tag{2.11}$$

with $c_0 = \frac{1}{2} - \gamma \approx -0.0772$ and γ being Euler's constant. In (2.10) $H(\cdot)$ denotes the Heaviside step function and primes denote differentiation with respect to σ. Detailed discussions of the operator and of its mathematical character are given by Klein & Majda (1991*a*, *b*).

These authors also show that Hasimoto's transform (Hasimoto 1972) turns (2.6) with $\boldsymbol{v}$ from (2.9) into the perturbed nonlinear–non-local Schrödinger equation

$$(1/i)\, \Psi_\tau = \Psi_{\tilde{\sigma}\tilde{\sigma}} + \epsilon^2(\tfrac{1}{2}|\Psi|^2\, \Psi - \mathrm{I}[\Psi]) \tag{2.12}$$

for the complex filament function

$$\Psi(\tilde{\sigma}, \tau) = \kappa(\tilde{\sigma}, \tau)\, \mathrm{e}^{\mathrm{i}\int [\epsilon T]\, \mathrm{d}\tilde{\sigma}}. \tag{2.13}$$

Here κ, and T respectively denote the curvature and torsion of the filament reference line, while $\tilde{\sigma} = \tilde{s}/\epsilon$, where $\tilde{s}$ is an arclength coordinate scaled with the characteristic radius of curvature, R, and satisfies $\tilde{s} = s(1 + O(\epsilon^2))$.

Hasimoto analysed the local induction approximation for vortex filament dynamics, i.e. he considered (2.6) with $\boldsymbol{v} \equiv 0$ (and a suitably rescaled time variable $\bar{t} = t/\epsilon^2$). For three-dimensional filament geometries characterized by a single radius-of-curvature lengthscale, R, Hasimoto found the cubic nonlinear Schrödinger equation for the filament function, which corresponds to (2.12) with the $\mathrm{I}[\cdot]$-operator removed and with $\epsilon \equiv 1$. The surprising observation from (2.12) is that for perturbed curves as in (2.7) the relevant filament evolution equation is a perturbation to the linear Schrödinger equation, where nonlinear and non-local effects directly compete in the perturbation term:

$$\epsilon^2(\tfrac{1}{2}|\Psi|^2\, \Psi - \mathrm{I}[\Psi]). \tag{2.14}$$

Thus, for perturbations of the filament geometry in the Klein–Majda regime, non-local contributions become as important as the nonlinear local induction effects. Also the non-local term $-\epsilon^2\mathrm{I}[\Psi]$ is responsible for filament self-stretching. Thus, in the present regime of short-wavelength perturbations of a straight slender vortex, there is a direct competition at the same perturbation order in ϵ between nonlinear effects and the non-local self-action capable of self-stretching. The mathematical features of (2.12) are discussed in detail by Klein & Majda (1991*b*) and it is shown that the term $-\epsilon^2\mathrm{I}[\Psi]$ is a highly singular perturbation of the linear Schrödinger equation – (2.12) with $\epsilon^2 \equiv 0$. Numerical solutions of (2.12) demonstrate the effect of this singular perturbation when it interacts with the cubic nonlinearity. The computations reveal that there is a

nonlinear energy transfer in wavenumber space from long to short wavelengths due to this nonlinear–non-local interaction.

In §5, we compare predictions of the Klein–Majda theory with numerical simulations of slender vortex dynamics using the standard and improved thin-tube vortex element schemes from §4. These computations serve as stringent mutual tests for these two fundamentally different approaches and a successful comparison will lend strong support to both. In particular, we will consider cases with ϵ as large as $\frac{1}{2}$, which corresponds to realistic ratios of the vortex core size and a characteristic filament radius of curvature, $\delta \approx 0.02$, following Crow (1970). This is also the range of values chosen in Klein & Majda (1991*b*, 1993) and Klein *et al.* (1992) for computational convenience.

3. Derivation of the filament equation of motion and asymptotic solution of the vorticity transport equation

As mentioned in the introduction, the analysis starts with an asymptotic evaluation of the three-dimensional Biot–Savart integral from (1.5) for points $\boldsymbol{X} = \boldsymbol{X}_1 = \boldsymbol{X}(\tilde{s}_1, t)$ on any of the curves $L'(t)$ in the inner $O(\delta^2)$ core of the vortex. For convenience, we discard the time dependence in the notation for the rest of this section, as time only enters as a parameter in the Biot–Savart integral. We adopt the time-dependent filament-attached coordinates $(r, \theta, \tilde{s})$ which are explained in figure 2. The arclength $\tilde{s}$ is used as the curve parameter and we define a circumferential angle in planes normal to the filament reference curve following Ting (1971) as

$$\theta = \varphi + \theta_0 \quad \text{where} \quad \theta_0 = \int_0^{\tilde{s}} T(\tilde{s})\,\mathrm{d}\tilde{s}. \tag{3.1}$$

Notice that θ_0 is precisely the torsion integral that appeared in the definition of the filament function in (2.13). This choice will be convenient in later calculations (see e.g. (3.5) below).

We split the integration over R^3 into a local and a non-local contribution according to

$$\boldsymbol{v}_{ind}(\boldsymbol{X}_1) = \frac{1}{4\pi}\left(\int_{R^3 \setminus B_1} \boldsymbol{F}(\boldsymbol{x}, \boldsymbol{X}_1)\,\mathrm{d}^3x + \int_{B_1} \boldsymbol{F}(\boldsymbol{x}, \boldsymbol{X}_1)\,\mathrm{d}^3x \right). \tag{3.2}$$

Here $\boldsymbol{F}(\boldsymbol{x}, \boldsymbol{X}_1)$ abbreviates the integrand from (1.5) and B_1 is a ball of radius δ_B around the point of reference $\boldsymbol{X}_1$ as sketched in figure 3. This radius δ_B is small compared to the geometric scales of the filament, while it is large compared to the vortex core size. Since we have normalized lengths with respect to a characteristic filament radius of curvature, δ_B should satisfy the limiting constraints $1 \gg \delta_B \gg \delta$. In fact, below we will need the somewhat more stringent restrictions

$$1 \gg \delta_B \gg \delta^{1/2}. \tag{3.3}$$

In the following we evaluate the two integrals in (3.2) separately, using asymptotic methods.

The inner integral

Within the ball B_1 all geometrical variations of the filament reference line are weak and they may be represented asymptotically by Taylor series expansions. Using the stretched radial and axial coordinates

$$\bar{r} = r/\delta \quad \text{and} \quad z = (1/\delta)(\tilde{s} - \tilde{s}_1), \tag{3.4}$$

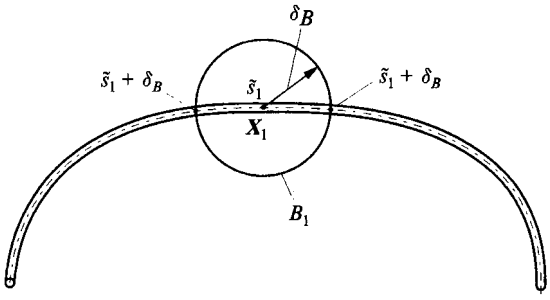

FIGURE 3. Local–non-local decomposition of the domain of integration for the asymptotic evaluation of the Biot–Savart integral.

one obtains

$$\boldsymbol{x}-\boldsymbol{X}_1 = \delta(z\boldsymbol{t}_1+\bar{r}\boldsymbol{e}_{r,1})+\delta^2(\tfrac{1}{2}z^2(\kappa\boldsymbol{b})_1-\bar{r}z\cos(\varphi)(\kappa\boldsymbol{t})_1)+O(\delta^3), \tag{3.5}$$

where subscript 1 denotes evaluation at $\tilde{s}=\tilde{s}_1$, the arclength coordinate of $\boldsymbol{X}_1$. To obtain (3.5) we have used the identity $\partial\boldsymbol{e}_r/\partial\tilde{s} = -\cos(\varphi)(\kappa\boldsymbol{t})$ for the arclength derivative of the radial unit vector $\boldsymbol{e}_r$. (The derivation uses the representation $\boldsymbol{e}_r = \cos(\varphi)\boldsymbol{n}+\sin(\varphi)\boldsymbol{b}$, the Serret–Frenet formulae (see Hasimoto 1972 or Klein & Majda 1991*a*) and, importantly, that $\partial/\partial\tilde{s}$ denotes a derivative at fixed (r,θ), but not at fixed (r,φ).) The vorticity is also expanded for small $\tilde{s}-\tilde{s}_1$ as

$$\begin{aligned}\boldsymbol{\omega} = {}& (1/\delta^2)(\eta_1^{(0)}\boldsymbol{e}_{\theta,1}+\zeta_1^{(0)}\boldsymbol{t}_1)\\ &+(1/\delta)\left(\xi_1^{(1)}\boldsymbol{e}_{r,1}+\eta_1^{(1)}\boldsymbol{e}_{\theta,1}+\zeta_1^{(1)}\boldsymbol{t}_1+z\frac{\partial}{\partial\tilde{s}}(\eta^{(0)}\boldsymbol{e}_\theta+\zeta^{(0)}\boldsymbol{t})_1\right)\\ &+O(1).\end{aligned} \tag{3.6}$$

Finally, the transformation to filament-attached coordinates induces the relation

$$\mathrm{d}^3x \leftrightarrow \delta^2\bar{r}(1-\delta\bar{r}\kappa\cos(\varphi))\,\mathrm{d}\bar{r}\,\mathrm{d}\theta\,\mathrm{d}\tilde{s} \tag{3.7}$$

for the space volume increment.

For the present calculations we adopt the usual assumption that the leading-order vorticities be axisymmetric, so that

$$\eta^{(0)} = \eta^{(0)}(\bar{r},\tilde{s},t), \quad \zeta^{(0)} = \zeta^{(0)}(\bar{r},\tilde{s},t), \tag{3.8}$$

whereas $\xi_1^{(1)}$, $\eta_1^{(1)}$ and $\zeta_1^{(1)}$ do depend on the circumferential coordinate θ. Inserting the expansions (3.5)–(3.7) into the second integral in (3.2), we find the first two terms of the induced velocity at $\boldsymbol{X}_1$ to be

$$\boldsymbol{v}_{inner}^{(0)} = w_1^{(0)}|_{\bar{r}=0}\,\boldsymbol{t}_1+O((\delta/\delta_B)^2) \tag{3.9}$$

and

$$\begin{aligned}\boldsymbol{v}_{inner}^{(1)} = {}& \boldsymbol{t}_1\langle w^{(1)}\rangle_1|_{\bar{r}=0}\\ &+(\kappa\boldsymbol{n})_1\frac{1}{4}\frac{1}{\kappa}\int_0^\infty\int_{-\delta_B/\delta}^{\delta_B/\delta}\frac{\bar{r}^2}{(\bar{r}^2+z^2)^{3/2}}[\zeta_{12}^{(1)}]_1\,\mathrm{d}z\,\mathrm{d}\bar{r}\\ &+(\kappa\boldsymbol{b})_1\frac{1}{4}\int_0^\infty\int_{-\delta_B/\delta}^{\delta_B/\delta}\frac{\bar{r}}{(\bar{r}^2+z^2)^{3/2}}\left[\left(\bar{r}^2+z^2-\frac{3}{2}\frac{\bar{r}^2z^2}{\bar{r}^2+z^2}\right)\zeta^{(0)}-\frac{\bar{r}}{\kappa}\zeta_{11}^{(1)}\right]_1\mathrm{d}z\,\mathrm{d}\bar{r}\\ &+o(1) \quad \text{as} \quad \delta_B/\delta\to\infty.\end{aligned} \tag{3.10}$$

Here the leading-order axial velocity, evaluated on the filament reference line,

$$w_1^{(0)}|_{\bar{r}=0} = \int_0^\infty \eta_1^{(0)}\,\mathrm{d}\bar{r}, \tag{3.11}$$

has been introduced; similarly, the circumferential average of the first-order axial velocity on the reference line $\langle w_1^{(1)}\rangle|_{\bar{r}=0}$ is given by

$$\langle w_1^{(1)}\rangle|_{\bar{r}=0} = \int_0^\infty \langle \eta_1^{(1)}\rangle\,\mathrm{d}\bar{r}, \tag{3.12}$$

where

$$\langle f\rangle = \frac{1}{2\pi}\int_0^{2\pi} f\,\mathrm{d}\theta. \tag{3.13}$$

Furthermore, $\zeta_{11}^{(1)}$ and $\zeta_{12}^{(1)}$ are Fourier components with respect to θ of the first-order vorticity, defined by

$$\zeta_{11}^{(1)} + \mathrm{i}\zeta_{12}^{(1)} = \frac{1}{\pi}\int_0^{2\pi} \zeta^{(1)}(\bar{r}, \theta, \tilde{s}_1, t)\,\mathrm{e}^{\mathrm{i}\theta}\,\mathrm{d}\theta. \tag{3.14}$$

Only the induced velocity components in planes normal to the filament reference line are of relevance for its geometrical evolution and, anticipating that $\zeta_{12}^{(1)} \equiv 0$ from the asymptotic solution of the vorticity transport equation below, we obtain for these components

$$\boldsymbol{v}_{inner}^{\perp} = \left\{\frac{\Gamma}{4\pi}\left[\ln\left(\frac{2\delta_B}{\delta}\right) - \frac{1}{2}\right] - \frac{1}{2}\int_0^\infty \left[\frac{1}{\kappa}\zeta_{11}^{(1)} + \bar{r}\ln\bar{r}\zeta^{(0)}\right]\mathrm{d}\bar{r}\right\}(\kappa\boldsymbol{b})_1 + o(1) \quad \text{as} \quad \delta_B/\delta \to \infty. \tag{3.15}$$

To arrive at this result, we have explicitly carried out the integrations over z in (3.10) and neglected terms of $O((\delta/\delta_B)^2)$ and smaller.

An important fact from (3.15) is the linear influence of the leading- and first-order vorticities on the induced velocity. This may have been expected, as the fundamental velocity–vorticity relation via the Biot–Savart integral is linear. On the other hand, this result at a first glance seems to contradict earlier theoretical considerations, e.g. by Callegari & Ting (1978), which predicted a nonlinear influence of the leading-order vortex core structure on the filament motion. We resolve this discrepancy later in this section by an asymptotic solution of the vorticity transport equation inside the vortex core which exhibits a nonlinear dependence of $\zeta_{11}^{(1)}$ and $\zeta_{12}^{(1)}$ on $\eta^{(0)}$ and $\zeta^{(0)}$.

The outer integration

Here we consider the first integral from (3.2), where $|\boldsymbol{x}-\boldsymbol{X}_1| \geqslant \delta_B$. In this regime we have

$$\boldsymbol{x}-\boldsymbol{X}_1 = (\boldsymbol{X}(\tilde{s})-\boldsymbol{X}(\tilde{s}_1)) + \delta\bar{r}\boldsymbol{e}_r(\theta, \tilde{s}) \tag{3.16}$$

and the asymptotic expansion of the integral yields

$$\boldsymbol{v}_{outer} = \frac{1}{4\pi}\int_{L\setminus I_B} \frac{\boldsymbol{X}(\tilde{s})-\boldsymbol{X}_1}{|\boldsymbol{X}(\tilde{s})-\boldsymbol{X}_1|^3} \times \int_0^\infty\int_0^{2\pi} \boldsymbol{\omega}^{(0)}\bar{r}\,\mathrm{d}\theta\,\mathrm{d}\bar{r}\,\mathrm{d}\tilde{s}\cdot(1+O(\delta)), \tag{3.17}$$

where I_B denotes the interval $\tilde{s}-\delta_B < \tilde{s} < \tilde{s}+\delta_B$. Using the asymptotic representation of the vorticity in (3.6) and taking into account that the leading-order vorticities are axisymmetric, the double integral in (3.17) at the leading-order evaluates to $\Gamma\boldsymbol{t}(\tilde{s})$ where Γ is the total circulation of the vortex and $\boldsymbol{t}$ is the local unit tangent to $L'(t)$. In this

fashion we obtain the standard line Biot–Savart integral with the arbitrary matching length δ_B as a cut-off

$$\boldsymbol{v}_{outer}(\boldsymbol{X}_1) = \frac{\Gamma}{4\pi}\int_{L'\setminus I_B} \frac{\boldsymbol{X}(\tilde{s})-\boldsymbol{X}_1}{|\boldsymbol{X}(\tilde{s})-\boldsymbol{X}_1|^3}\times \boldsymbol{t}(s)\,\mathrm{d}\tilde{s}\cdot(1+O(\delta)). \tag{3.18}$$

This expression is logarithmically singular as δ_B vanishes and we extract the structure of this singular behaviour by analysing the immediate vicinity of the reference point. In this region, one may expand the integrand from (3.18) as

$$\hat{\boldsymbol{F}}(\tilde{s}) = \frac{\boldsymbol{X}(\tilde{s})-\boldsymbol{X}_1}{|\boldsymbol{X}(\tilde{s})-\boldsymbol{X}_1|^3}\times \boldsymbol{t} = \hat{\boldsymbol{F}}_1(\tilde{s})+O(1) \quad \text{as} \quad \tilde{s}-\tilde{s}_1\to 0, \tag{3.19a}$$

where the local representation of the integrand is

$$\hat{\boldsymbol{F}}_1(\tilde{s}) = \frac{1}{2}\frac{1}{|\tilde{s}-\tilde{s}_1|}(\kappa\boldsymbol{b})_1. \tag{3.19b}$$

Recalling that only the normal components of the induced velocity are relevant for the geometrical evolution of the filament geometry, we may now write

$$\boldsymbol{v}^{\perp}_{outer} = \frac{\Gamma}{4\pi}\ln\left(\frac{\rho}{\delta_B}\right)(\kappa\boldsymbol{b})_1 + \boldsymbol{Q}^{f\,\perp}_{\rho}, \tag{3.20}$$

where $\boldsymbol{Q}^{f\,\perp}_{\rho} = \boldsymbol{Q}^{f}_{\rho}(\boldsymbol{1}-\boldsymbol{t}\circ\boldsymbol{t})$ is the component normal to $\boldsymbol{t}$ of the non-local finite part of the Biot–Savart integral $\boldsymbol{Q}^{f}_{\rho}$ which is defined by

$$\boldsymbol{Q}^{f}_{\rho} = \int_L \hat{\boldsymbol{F}}(\tilde{s}) - H\left(1-\frac{|\tilde{s}-\tilde{s}_1|}{\rho}\right)\boldsymbol{F}_1(\tilde{s})\,\mathrm{d}\tilde{s}. \tag{3.21}$$

Here $H(s)$ is the Heaviside step function and ρ is a length comparable with the characteristic length of the filament geometry. Notice that the choice of ρ has absolutely no influence on the result of (3.20). It may conveniently be set to unity, which would produce a slight simplification of the formulae. However, for the Klein–Majda regime discussed above the appropriate choice is $\rho = \epsilon$ and it is in fact this choice which, in a straightforward manner, leads to the definition of the I-operator in (2.10), (2.11). Collecting the contributions from the inner and outer integration of (3.15), (3.20) and (3.21) we obtain

$$\boldsymbol{v}^{\perp} = \frac{\Gamma}{4\pi}\left(\ln\left(\frac{2\rho}{\delta}\right)+C\right)(\kappa\boldsymbol{b})_1 + \boldsymbol{Q}^{f\,\perp}_{\rho}, \tag{3.22}$$

where

$$C = -\left(\frac{1}{2}+\frac{2\pi}{\Gamma}\int_0^{\infty}\left[\frac{1}{\kappa}\zeta^{(1)}_{11}+\bar{r}\ln\bar{r}\,\zeta^{(0)}\right]\mathrm{d}\bar{r}\right). \tag{3.23}$$

This is the formulation for the filament velocity announced in (2.6), (2.9) when we let $\rho = \epsilon$ and $\boldsymbol{v} = \boldsymbol{Q}^{f\,\perp}_{\rho}$. However, to complete the derivation of the induced velocity at points on $L'(t)$ in terms of the filament geometry and of the leading-order vortex core structure, we need to eliminate $\zeta^{(1)}_{11}$. This is done in the subsequent calculation where we analyse the asymptotic solution of the vorticity transport equation in the vortex core region.

We observe here that the formulae in (3.22) and (3.23) are valid for any curve $L'(t)$ located in the inner $O(\delta^2)$ core of the vortex, since in the attached frames of all of these curves one finds the same axisymmetric leading-order vorticity distribution. The only

difference between the induced velocities on two such curves stems from differences in $\zeta_{11}^{(1)}$. In the subsequent asymptotic analysis of the vorticity transport equation inside the vortex core, we compute the very distribution of $\zeta_{11}^{(1)}$ valid for $L' \equiv L^{st}(t)$, i.e. for the connecting line of stagnation points in the moving frame of reference. By inserting the result in (3.23) we obtain the desired value of the core coefficient that determines the filament motion.

Asymptotic solution of the vorticity transport equation

For the computations of this section it is convenient to split the local flow velocity into the sum of the relative velocity in the filament attached frame of reference plus the velocity of the filament reference line. We let

$$\boldsymbol{v} = \boldsymbol{X}_t + \boldsymbol{V}, \tag{3.24}$$

where $\boldsymbol{V}$ has the asymptotic representation

$$\boldsymbol{V} = \frac{1}{\delta}(v^{(0)}\boldsymbol{e}_\theta + w^{(0)}\boldsymbol{t}) + (u^{(1)}\boldsymbol{e}_r + v^{(1)}\boldsymbol{e}_\theta + w^{(1)}\boldsymbol{t}) + O(\delta). \tag{3.25}$$

Here $\boldsymbol{V}$ has axisymmetric leading-order components $v^{(0)}$ and $w^{(0)}$, while the first-order contributions $u^{(1)}$, $v^{(1)}$ and $w^{(1)}$ depend non-trivially on the circumferential coordinate θ. Insertion of (3.6) and (3.25) into the vorticity transport equation in (1.4) first shows that the leading two terms in δ express a balance of vorticity advection and vortex stretching. Thus,

$$(\boldsymbol{V}\cdot\boldsymbol{\nabla})\boldsymbol{\omega} = (\boldsymbol{\omega}\cdot\boldsymbol{\nabla})\,\boldsymbol{V}\cdot(1+O(\delta^2)). \tag{3.26}$$

To arrive at this result it is crucial to assume a quasi-steady solution for the core structure, i.e. no changes on timescales shorter than $t_{ref} = 4\pi R^2/\Gamma$. Then the time derivative terms are small and enter at higher order only. Using the stretched radial coordinate $\bar{r}$ from (3.4), the gradient operator in terms of filament attached coordinates reads

$$\boldsymbol{\nabla} = \frac{1}{\delta}\left(\boldsymbol{e}_r\,\partial_{\bar{r}} + \frac{1}{\bar{r}}\boldsymbol{e}_\theta\,\partial_\theta\right) + \boldsymbol{t}\,\partial_{\tilde{s}}, \tag{3.27}$$

and (3.6), (3.25) and (3.27) inserted in (3.26) readily yield the leading- and first-order vorticity transport equations valid in the vortex core region. It turns out that the leading-order equations are trivially solved for any arbitrary axisymmetric leading-order core structure. At the first order, we are interested only in the equation for the axial vorticity component $\xi^{(1)}$. We thus consider the axial component of the vorticity transport equation, eliminate $\xi^{(1)}$ by using the identity

$$\xi^{(1)} = (1/\bar{r})\,w_\theta^{(1)} + \kappa\sin(\varphi)\,w^{(0)}, \tag{3.28}$$

which can be derived from the definition of the vorticity as the curl of velocity, and find

$$v^{(0)}\zeta_\theta^{(1)} + \bar{r}u_{\bar{r}}^{(1)}\,\zeta_{\bar{r}}^{(0)} + \bar{r}\kappa\sin(\varphi)(\zeta^{(0)}v^{(0)} - 2w^{(0)}\eta^{(0)}) = 0. \tag{3.29}$$

Multiplication by $e^{i\theta}$ and integration immediately yields

$$\zeta_{11}^{(1)} = \frac{\bar{r}\zeta_{\bar{r}}^{(0)}}{v^{(0)}}u_{12}^{(1)} + \bar{r}\kappa\left(\zeta^{(0)} - \frac{(w^{(0)^2})_{\bar{r}}}{v^{(0)}}\right) \quad \text{and} \quad \zeta_{12}^{(1)} \equiv \frac{\bar{r}\zeta_{\bar{r}}^{(0)}}{v^{(0)}}u_{11}^{(1)}, \tag{3.30}$$

if one takes into account that $\eta^{(0)} \equiv w_{\bar{r}}^{(0)}$.

By introducing a suitable streamfunction for the first-order flow in planes normal to the filament reference line, one can show that (3.29) is equivalent to the streamfunction

equation (4.18) of Callegari & Ting (1978) or (4.21) of Klein & Majda (1991*a*), for which explicit solutions in terms of the leading-order core structure are available. As explained earlier in this section and in the introduction, we seek the induced velocity at the local stagnation point in the filament-attached frame of reference, so that we must require that $u^{(1)}$ and $v^{(1)}$ both vanish at $\bar{r} = 0$. Although we have used a totally different argument than that employed in the references cited, we arrive at the same inner boundary conditions for the streamfunction equation and may therefore directly use the solutions for the first-order flow which are given in these studies. Thus, we find

$$\bar{r}u_{12}^{(1)} = -\kappa v^{(0)} \int_0^{\bar{r}} \frac{1}{r' v^{(0)^2}} \int_0^{r'} r'' v^{(0)} H^{(0)} \, dr'' \, dr', \tag{3.31}$$

where

$$v^{(0)} H^{(0)} = 2\bar{r} v^{(0)} \zeta^{(0)} + v^{(0)^2} + 2\bar{r} w^{(0)} w_{\bar{r}}^{(0)}. \tag{3.32}$$

By combining (3.23) with (3.30)–(3.32) we obtain the desired expression for the core structure coefficient, namely

$$C = \lim_{r \to \infty} \left(\frac{4\pi^2}{\Gamma^2} \int_0^{\bar{r}} r' v^{(0)^2} \, dr' - \ln \bar{r} \right) - \tfrac{1}{2} - \frac{8\pi^2}{\Gamma^2} \int_0^{\infty} r' w^{(0)^2} \, dr'. \tag{3.33}$$

This completes the new derivation of the equation of motion of a slender vortex filament.

4. Thin-tube vortex element schemes

4.1. *The standard thin-tube model*

Construction of the three-dimensional vortex filament model starts with the discretization of the slender vortex into a finite number of vortex elements. Each element is specified in terms of the circulation Γ of the filament and two Lagrangian variables which describe the endpoints of a material segment that is located close to the centre of the vortex. The Lagrangian variables are denoted $\boldsymbol{\chi}_i$, $i = 1, \ldots, N$, where N is the total number of vortex elements. The latter are ordered so that the indices increase in the direction of the vorticity vector. Thus, the collection $\{\boldsymbol{\chi}_i\}_{i=1}^N$ defines a directed graph which constitutes a discrete approximation to the filament geometry. We will call the $\{\boldsymbol{\chi}_i\}_{i=1}^N$ *vortex element nodes*, or simply *nodes*, from here on.

Based on the node locations, a smooth numerical approximation of the filament vorticity is defined using the expression (Beale & Majda 1985, 1982*a*, *b*; Greengard 1986):

$$\boldsymbol{\omega}(\boldsymbol{x}, t) = \sum_{i=1}^{N} \Gamma \delta \boldsymbol{\chi}_i(t) f_\delta(\boldsymbol{x} - \boldsymbol{\chi}_i^c(t)), \tag{4.1}$$

where Γ is the circulation of the filament, and

$$\delta \boldsymbol{\chi}_i(t) = \boldsymbol{\chi}_{i+1}(t) - \boldsymbol{\chi}_i(t), \tag{4.2}$$

$$\boldsymbol{\chi}_i^c(t) = \tfrac{1}{2}(\boldsymbol{\chi}_{i+1}(t) + \boldsymbol{\chi}_i(t)) \tag{4.3}$$

respectively denote the length and centre of the ith vortex element. In (4.1), f_δ represents a rapidly decreasing spherical core smoothing function of unit mass which obeys the relationship

$$f_\delta(\boldsymbol{x}) = \frac{1}{\delta^3} f\left(\frac{|\boldsymbol{x}|}{\delta} \right). \tag{4.4}$$

Importantly, in the standard thin-tube approach it is implicitly assumed that the numerical core size parameter δ^{ttm} coincides with the physical characteristic vortex core diameter δ, which is why we are not making any distinction of notation in this summary of the standard scheme. See, however, the third correction method for the model described below, where we do introduce an explicit choice of δ^{ttm} that differs from the physical quantity δ.

Following Beale & Majda (1985), the smoothing function is required to satisfy certain moment constraints which ensure that the velocity induced by a vortex element is non-singular but asymptotically approaches that of a concentrated vortex for distances larger than the core radius δ, which directly corresponds to the characteristic physical vortex core size introduced in the preceding section. The discretization of the filament geometry further obeys the requirement of overlapping cores, a condition that is widely assumed in the vortex element convergence studies cited above. In particular, the maximum separation between neighbouring elements should be smaller than the core size, i.e. $\max\{|\delta\boldsymbol{\chi}_i(t)|\}_{i=1}^{N} < \delta$.

This construction, which resembles those used by Chorin (1980) and Knio & Ghoniem (1990) enables us to follow vortex element methodologies. Thus, the velocity field may be simply reconstructed by inserting (4.1) into (1.5). The result is the following desingularized Biot–Savart law:

$$\boldsymbol{v}^{ttm}(\boldsymbol{x}, t) = -\frac{\Gamma}{4\pi}\sum_{i=1}^{N}\frac{(\boldsymbol{x}-\boldsymbol{\chi}_i^c(t))\times\delta\boldsymbol{\chi}_i(t)}{|\boldsymbol{x}-\boldsymbol{\chi}_i^c(t)|^3}\kappa_\delta(\boldsymbol{x}-\boldsymbol{\chi}_i^c(t)), \tag{4.5}$$

where

$$\kappa_\delta(\boldsymbol{x}) \equiv \kappa(|\boldsymbol{x}|/\delta); \quad \kappa(r) = 4\pi\int_0^r \xi^2 f(\xi)\,\mathrm{d}\xi \tag{4.6}$$

is the velocity smoothing kernel corresponding to f_δ.

When coupled with this desingularized velocity field representation, the adopted Lagrangian representation of the vortex elements allows straightforward discrete approximation of solutions of the governing equations. We first recall that the vortex elements are represented by Lagrangian nodes, whose motion obeys

$$\mathrm{d}\boldsymbol{\chi}_i(t)/\mathrm{d}t = \boldsymbol{u}_i \equiv \boldsymbol{v}^{ttm}(\boldsymbol{\chi}_i(t), t). \tag{4.7}$$

Next, we invoke the theorems of Kelvin and Helmholtz to conclude that the circulation of the filament remains constant, while the filament vorticity changes according to local stretching and tilting of its reference line. Since the latter is described by the Lagrangian locations of the elements, stretching and tilting effects are implicitly accounted for in the vorticity representation in (4.1)–(4.3). Thus, the vorticity transport equation is implicitly accounted for and an explicit evaluation of velocity gradients is avoided. In the present computations, a second-order predictor-corrector scheme is used to integrate the system in (4.7). The present implementation of the thin-tube model incorporates a mesh refinement scheme analogous to that used by Knio & Ghoniem (1990). Remeshing occurs when the length of a single element excedes a pre-chosen threshold. A single element is divided into two by inserting a new Lagrangian variable at the midpoint of the associated segment whenever $\delta\chi > 0.4\delta$. Thus, the redistribution scheme ensures that a sufficient core overlap among neighbouring elements is always maintained. The incorporation of such a redistribution scheme has been shown by Ghoniem, Heidarinejad & Krishnan (1988) and by Knio & Ghoniem (1990, 1991) to guard against potential deterioration of the accuracy of the discretization due to severe deformation of the Lagrangian mesh by prevailing strain.

Further distinctive features of the present thin-tube model computations are a

spectral representation of the filament geometry, an associated nonlinear filtering in Fourier space and the treatment of periodic boundary conditions. We defer the detailed explanation of these techniques to §6.2 and Appendix A.

4.2. *Asymptotic corrections of the thin-tube model*

The fundamental idea underlying the thin-tube model is to move the vortex element nodes with velocities based on an *exact* evaluation of the Biot–Savart integral for an *approximate* numerical vorticity distribution. Through a suitable choice of the numerical core smoothing function $f_\delta(r)$ and by identifying the numerical core size parameter δ, a wide range of vorticity distributions can be represented by the numerical approximation. It is then assumed that the induced velocity at the nodes is a good approximation to the local filament velocity. This assumption turns out to be wrong and this can be seen through the following argument.

In the thin-tube model, the numerical vorticity distribution has filament structure, so that the asymptotic analysis of the Biot–Savart integral from §3 may directly be applied to obtain an analytical representation of the numerical induced velocity for sufficiently small δ. Let $(\zeta^{(0)}, \zeta_{11}^{(1)})$ and $(\zeta^{(0),ttm}, \zeta_{11}^{(1),ttm})$ be the physical and numerical vorticity components needed in the velocity formulae (3.22), (3.23), respectively. Assume further that, at a given time, the vortex element nodes lie in the inner $O(\delta^2)$ core of the filament. Then, according to (3.21), the non-local parts of the induced velocities $\boldsymbol{Q}_\rho^I$ coincide. However, a difference exists between the node velocity in the thin-tube model and the correct filament velocity owing to differences in the physical and the numerical core coefficients, C and C^{ttm}, computed from (3.23). Hence an error of order unity in the predicted numerical node velocity occurs.

In the next subsection, we will derive suitable expressions for $\zeta^{(0),ttm}, \zeta_{11}^{(1),ttm}$ by means of an asymptotic analysis of the *numerical* vorticity structure. Until then, we assume these functions to be given explicitly and concentrate on how to modify the thin-tube model in order to remove possible $O(1)$ deviations between the numerical and the asymptotically correct filament velocity predictions.

We discuss three independent correction strategies. The first is based on adding an explicit correction velocity to the numerical node velocity from the standard method. The second relies on an exact evaluation of the three-dimensional Biot–Savart integral, but at corrected locations that are displaced from the vortex element nodes by an $O(\delta^2)$ shift. In the third correction method, we no longer identify the numerical core radius, δ^{ttm}, with the filament core size, δ; instead, δ^{ttm} is appropriately rescaled so as to produce the correct local induction effects.

I. Explicit correction velocities

Assume that the leading-order axisymmetric core structure of a vortex is given and that explicit representations of the vorticity components $\zeta^{(0),ttm}, \zeta_{11}^{(1),ttm}$ have been derived based on the numerical approximate vorticity distribution through a suitable asymptotic analysis. Then, in order to move the vortex element nodes with a velocity correct to $O(\delta)$, we use the asymptotic representation of the induced velocity from (3.22) and let

$$\boldsymbol{v}_{node}^{corr} = \boldsymbol{v}_{node} + \frac{\Gamma}{4\pi}(\kappa \boldsymbol{b})\,[C - C^{ttm}], \tag{4.8}$$

where C is the core structure coefficient from (3.23) evaluated with the physical vorticity components $\zeta^{(0)}, \zeta_{11}^{(1)}$, while C^{ttm} is its analogue based on the numerical vorticity distribution, i.e. evaluated using $\zeta^{(0),ttm}, \zeta_{11}^{(1),ttm}$.

II. Evaluation of the Biot–Savart integral at corrected locations

It has been emphasized earlier that the desired filament velocity equals the induced velocity on the connecting line of stagnations points in the inner $O(\delta^2)$-core of the filament, except for an axial velocity component that is irrelevant for the geometrical evolution of the vortex reference line. If we are able to compute a node-to-stagnation-point displacement in the normal planes of the vortex, then in order to obtain the correct motion of a vortex element node we just have to: (i) evaluate the Biot–Savart integral for the stagnation point closest to the node and (ii) propagate the node with this induced velocity.

Below, this node-to-stagnation-point displacement is determined based on the physical and numerical vorticity components $\zeta^{(0)}, \zeta_{11}^{(1)}$ and $\zeta^{(0),ttm}, \zeta_{11}^{(1),ttm}$. The key observation is that the nodes and stagnation points are displaced from each other by a distance of $O(\delta^2)$. Since the characteristic transverse scale of the vorticity and velocity distributions is much larger, namely of $O(\delta)$, a Taylor series expansion may be used to express the induced velocity at a stagnation point, given the velocity at a node:

$$\boldsymbol{v}_{stagn} = \boldsymbol{v}_{node} + \delta^2 z \boldsymbol{n} \cdot (\nabla \boldsymbol{v})_{\bar{r}=0}. \tag{4.9}$$

Here we have anticipated a result of the next subsection, which says that the desired displacement is along the principal normal of the filament reference line. We now compute the scaled distance z.

Using the asymptotic representation of the induced velocity at points in the inner $O(\delta^2)$ core of the vortex from (3.22), (3.23) and the gradient operator (3.27) we find

$$\delta^2 \boldsymbol{n} \cdot (\nabla \boldsymbol{v})_{\bar{r}=0} = \tfrac{1}{2} \zeta^{(0),ttm}|_{\bar{r}=0} \boldsymbol{b}. \tag{4.10}$$

We combine (4.9), (4.10) with (4.8) to obtain

$$z = \frac{\Gamma \kappa}{2\pi} \frac{C - C^{ttm}}{\zeta^{(0),ttm}|_{\bar{r}=0}}. \tag{4.11}$$

In summary, the idea for the second approach to correcting the thin-tube vortex element model is to

(i) compute the node-to-stagnation-point distance z from (4.11) using (3.23) and the explicit representations of $\zeta^{(0),ttm}, \zeta_{11}^{(1),ttm}$ to be derived in the next subsection,

(ii) evaluate the Biot–Savart integral based on the numerical vorticity distribution for the stagnation points

$$\boldsymbol{X}_{stagn} = \boldsymbol{X}_{node} + \delta^2 z \boldsymbol{n}, \tag{4.12}$$

to obtain the induced velocity $\boldsymbol{v}_{stagn}$, and

(iii) integrate $\mathrm{d}\boldsymbol{\chi}_i/\mathrm{d}t = \boldsymbol{v}_{stag}(\boldsymbol{\chi}_i)$.

III. Rescaled numerical core radius

The third and, from a practical point of view, simplest and most efficient asymptotic correction is a suitable rescaling of the numerical core radius δ^{ttm}. Following the arguments in §§3 and 4.3, the *numerical* induced velocity at the nodes has the asymptotic representation

$$\boldsymbol{X}_t^{ttm} = \frac{\Gamma}{4\pi}\left(\ln \frac{2}{\delta^{ttm}} + C^{ttm}\right) \kappa \boldsymbol{b} + \boldsymbol{Q}^{f,\perp}, \tag{4.13}$$

which is formally analogous to the asymptotic formula for the physical filament velocity (3.22). For the third correction, we allow deviations from the original assumption of the thin-tube model that the numerical core radius matches the physical one. Thus, we apply the *standard* thin-tube model using a rescaled numerical core radius, chosen so as to satisfy

$$\ln\frac{2}{\delta^{ttm}}+C^{ttm}=\ln\frac{2}{\delta}+C, \tag{4.14}$$

or equivalently,

$$\delta^{ttm}=\delta\exp(C^{ttm}-C). \tag{4.15}$$

This rescaling guarantees that the asymptotic representations of the numerical and physical filament velocities coincide except for local errors of $O(\delta)$ as $\delta\to 0$. As pointed out earlier, the non-local contributions match except for very small numerical discretization errors.

This third corrected thin-tube model is easy to implement since it does not involve the computational of higher-order arclength derivatives of the filament geometry, which is necessary in the first and second correction methods. However, we caution that a successful application of this method including qualitative and quantitative comparison between theoretical and numerical predictions requires a very careful distinction of the numerical and physical core size parameters.

4.3. *Asymptotic structure of the numerical vorticity distribution*

The numerical vorticity distribution from (4.1)–(4.4) approximates the following smooth superposition of spherical blobs of vorticity:

$$\boldsymbol{\omega}^{ttm}(\boldsymbol{X},t)=\Gamma\int_{L^{ttm}(t)}f_\delta(|\boldsymbol{X}-\boldsymbol{X}^{ttm}(\tilde{s},t)|)\,\boldsymbol{t}(\tilde{s},t)\,\mathrm{d}\tilde{s}, \tag{4.16}$$

where $L^{ttm}(t)$ is a smooth curve connecting the vortex element nodes. When the vorticity distribution from (4.16) has filament structure, i.e. when $\delta/R\ll 1$, with R being a typical filament radius of curvature, then an asymptotic evaluation of (4.16) similar to the computation of the Biot–Savart integral in §2 is possible.

In analogy to the inner–outer decomposition of the Biot–Savart integral in (3.2), we rewrite (4.16) as

$$\boldsymbol{\omega}^{ttm}(\boldsymbol{X},t)=\Gamma\left(\int_{L^{ttm}(t)\setminus I_B}f_\delta\boldsymbol{t}\,\mathrm{d}\tilde{s}+\int_{I_B}f_\delta\boldsymbol{t}\,\mathrm{d}\tilde{s}\right)+\ldots, \tag{4.17}$$

where I_B is the same interval as introduced in (3.17). The numerical vorticity smoothing function $f_\delta(r)$ is rapidly decaying for $r/\delta\gg 1$, so that the contribution from the first integral in (4.17) is exponentially small as $\delta_B/\delta\to\infty$. For the second integral, the curve geometry may be expanded as in (3.5). By this approach we have

$$\left.\begin{aligned}\boldsymbol{X}-\boldsymbol{X}^{ttm}(\tilde{s},t)&=\delta(\bar{r}\boldsymbol{e}_{r,1}+z\boldsymbol{t}_1)+\delta^2\frac{z^2}{2}(\kappa\boldsymbol{n})_1+\ldots,\\ \boldsymbol{t}(\tilde{s},t)&=\boldsymbol{t}_1+\delta z(\kappa\boldsymbol{n})_1+\ldots,\end{aligned}\right\} \tag{4.18}$$

where the stretched coordinates $\bar{r}$ and z from (3.4) have been employed. Subscript 1 denotes evaluation at $\tilde{s}_1$, which is the arclength coordinate of the point $\boldsymbol{X}_1^{ttm}$ on the numerical filament reference line $L^{ttm}(t)$ that is closest to the point of reference $\boldsymbol{X}$.

Using the expansion from (4.18) and the explicit representation of $f_\delta(r)$ in (4.4) one finds

$$f_\delta(|\boldsymbol{X}-\boldsymbol{X}^{ttm}(\tilde{s},t)|)\,\boldsymbol{t}(\tilde{s},t)=f(R)\,\boldsymbol{t}_1+\delta\kappa\left[zf(R)\,\boldsymbol{n}_1+\tfrac{1}{2}\cos\varphi\frac{\bar{r}z^2}{R}f'(R)\,\boldsymbol{t}_1\right]+O(\delta^2), \quad (4.19)$$

where
$$R=(\bar{r}^2+z^2)^{1/2}, \quad (4.20)$$

and a prime denotes differentiation. Inserting this expansion in (4.16) and integrating with respect to z, we find the following asymptotic representation of the thin-tube vorticity distribution:

$$\boldsymbol{\omega}^{ttm}=\frac{1}{\delta^2}(\zeta^{(0),ttm}(\bar{r})+\delta\cos\varphi\zeta_{11}^{(1),ttm}(\bar{r}))\,\boldsymbol{t}_1\cdot(1+O(\delta\delta_B,f(\delta_B/\delta))), \quad (4.21)$$

where $\zeta^{(0),ttm}$ and $\zeta_{11}^{(1),ttm}$ are given by

$$\zeta^{(0),ttm}(\bar{r})=\Gamma\int_{-\infty}^{\infty}f(\bar{r}^2+z^2)^{1/2}\,\mathrm{d}z \quad (4.22)$$

and
$$\zeta_{11}^{(1),ttm}(\bar{r})=\frac{\Gamma\kappa}{2}\int_{-\infty}^{\infty}\frac{\bar{r}z^2}{(\bar{r}^2+z^2)^{1/2}}f'(\bar{r}^2+z^2)^{1/2}\,\mathrm{d}z. \quad (4.23)$$

These are the desired numerical vorticity components that enter the formulae for the induced velocity at the vortex element nodes from (3.22) and (3.23) as explained in §4.2. Given a suitable numerical vortex core smoothing function, the formulae in (4.22), (4.23) can be evaluated and the numerical core structure coefficient C^{ttm}, needed for the improved thin-tube models of §3.2, can be computed from (3.23). We notice that the leading-order distribution $\zeta^{(0),ttm}(\bar{r})$ is constant in time and does not vary along the filament curve. It is determined completely by the core smoothing function. The numerical first-order vorticity component $\zeta_{11}^{(1),ttm}$ is proportional to the filament curvature just as the corresponding physical component $\zeta_{11}^{(1)}$ from (3.30)–(3.32). Notice, however, that their radial distributions are totally different. While that of $\zeta_{11}^{(1),ttm}$ is again determined completely as a linear functional of the numerical core smoothing function, $\zeta_{11}^{(1)}$ has been obtained from the asymptotic solution of the vorticity transport equation and it depends nonlinearly on the physical leading-order vorticity.

4.4. *A spectral variant of the thin-tube model*

Numerical implementation of the corrected thin-tube models discussed in §4.2 above require, in particular, that the local curvature of the filament reference line be estimated during the computations, as well as its local tangent, normal and binormal vectors. However, numerical estimates of the desired quantities may not be simple to obtain in conjunction with the standard straight-segment-type reference line approximation described above. Furthermore, a careful numerical implementation must avoid compounding the stiffness of the equations with numerical accuracy problems associated with multiple differentiation of Lagrangian data.

In order to overcome these problems while at the same time obtaining accurate estimates of the desired derivative quantities, an improved variant of the thin-tube model is constructed. Briefly, this variant takes advantage of the periodic nature of the targeted perturbations by using the initial parametrization variable s as Lagrangian variable. This allows a 'spectral' interpolation of the filament geometry, which is incorporated in the present variant of the thin-tube model by processing the Lagrangian nodal locations with a discrete fast Fourier transform (FFT) routine. The

resulting Fourier coefficients are then used to estimate the first and second spectral (collocation) derivatives of the Lagrangian nodal coordinates with respect to s, $\boldsymbol{r}_i'(t) \equiv \partial\boldsymbol{\chi}(s,t)/\partial s|_{s_i}$ and $\boldsymbol{r}_i''(t) \equiv \partial^2\boldsymbol{\chi}(s,t)/\partial s^2|_{s_i}$. Once $\boldsymbol{r}'$ and $\boldsymbol{r}''$ are computed, the tangent, normal, binormal and curvature of the filament reference line are respectively evaluated using

$$\boldsymbol{t} = \boldsymbol{r}'/(\boldsymbol{r}'\cdot\boldsymbol{r}')^{1/2}, \tag{4.24}$$

$$\boldsymbol{n} = \frac{1}{\kappa}\left[\frac{\boldsymbol{r}''}{\boldsymbol{r}'\cdot\boldsymbol{r}'} - \frac{\boldsymbol{r}'\cdot\boldsymbol{r}''}{(\boldsymbol{r}'\cdot\boldsymbol{r}')^2}\boldsymbol{r}'\right], \tag{4.25}$$

$$\boldsymbol{b} = \boldsymbol{t}\times\boldsymbol{n} \tag{4.26}$$

and

$$\kappa = \frac{[(\boldsymbol{r}''\cdot\boldsymbol{r}'')(\boldsymbol{r}'\cdot\boldsymbol{r}') - (\boldsymbol{r}'\cdot\boldsymbol{r}'')^2]^{1/2}}{(\boldsymbol{r}'\cdot\boldsymbol{r}')^{3/2}}. \tag{4.27}$$

It should be mentioned, however, that since the components of the Lagrangian nodal locations are no periodic 'signals', spectral processing of the corresponding data should be carefully performed. This difficulty is overcome by first noting that for a filament that is L-periodic along the x-direction, the y- and z-components of the nodal locations are naturally L-periodic and may therefore be directly Fourier transformed. For the non-periodic x-component, we first form the L-periodic difference between current and initial values, and then take the Fourier transform of this difference. Since derivatives of the initial locations are known exactly, spectrally accurate derivatives of the non-periodic components can be easily deduced.

We also take advantage of the spectral decomposition of the reference line geometry in deriving a more accurate line Biot–Savart quadrature. To this end, we first modify the Lagrangian particle representation of the vorticity field and replace (4.1) by

$$\omega(\boldsymbol{x},t) = \sum_{i=1}^{N} \Gamma\delta\boldsymbol{\chi}_i(t) f_\delta(\boldsymbol{x}-\boldsymbol{\chi}_i(t)). \tag{4.28}$$

Meanwhile, the length of vortex elements is approximated using the spectral collocation derivative of the filament reference line, i.e. through

$$\delta\boldsymbol{\chi}_i(t) = \boldsymbol{r}_i'(t)\,\Delta s. \tag{4.29}$$

Accordingly, the desingularized line Biot–Savart integral is re-expressed as

$$\boldsymbol{v}^{ttm}(\boldsymbol{x},t) = -\frac{\Gamma}{4\pi}\sum_{i=1}^{N}\frac{(\boldsymbol{x}-\boldsymbol{\chi}_i(t))\times\delta\boldsymbol{\chi}_i(t)}{|\boldsymbol{x}-\boldsymbol{\chi}_i(t)|^3}\kappa_\delta(\boldsymbol{x}-\boldsymbol{\chi}_i(t)). \tag{4.30}$$

Thus, in this version of the numerical scheme, all derivatives are approximated by their corresponding spectral collocation derivatives. The remaining features of the algorithm, which deal primarily with Lagrangian tracking of the elements, are unaffected. As discussed below, the present modifications result in an improvement in an accuracy of the computations, without any appreciable increase in the computational overhead.

5. Slender vortices in the Klein–Majda regime

In this section we compare predictions for the evolution of slender vortex filaments obtained by the Klein & Majda (1991*a*) asymptotics with those generated by the thin-tube vortex element models of Knio & Ghoniem (1990) and of §4 of this paper. Vortex filaments in the Klein–Majda regime are particularly suited for a test of the thin-tube

models, because on the relevant timescales the vortex core structure is frozen. This fits in with the fact that the thin-tube models assume, in their current version, a time-independent numerical vorticity smoothing function. (As shown in §4, the corresponding leading-order structure also turns out to be frozen.) All the numerical predictions of this section have been generated with the spectral version of the thin-tube code as described in §4.4 and with $N = 1024$ nodes. In §6 we address several numerical issues and show, in particular, that the results obtained using the spectral representation of the filament geometry are in fact converged.

To explain what may be expected from this comparison, we first recall that the correct expression (3.22) for the filament velocity may be separated into the *local* binormal term and the *non-local* finite part of the Biot–Savart integral. Then we notice the following.

(I) The Klein–Majda (K & M) asymptotics
- \+ approximates the *local* contribution asymptotically accurate with errors of $O(\delta)$, while it
- − approximates the *non-local* term by the linearization from (2.9), (2.10) which involves errors of $O(\epsilon)$ as $\delta \to 0$, where ϵ is comparable to $1/\ln(1/\delta)$ according to the definition in (1.12).

On the other hand, we observe that

(II) the standard thin-tube model
- − mis-predicts the *local* contribution with errors of $O(1)$, while it
- \+ provides highly accurate predictions for the *non-local* part.

Through our efforts described in §§2–4 we have removed the gross local error of the thin-tube model. In fact, with either of the proposed corrections the numerical method inherits the accuracy of the asymptotic analysis as regards the local binormal term. In this sense, we have used the systematic asymptotic analysis in order to fine-tune the numerical model. As a consequence, we observe that

(III) the corrected thin-tube models from §4
- \+ approximate the *local* contribution asymptotically accurate with errors of $O(\delta)$, while they
- \+ provide highly accurate predictions for the *non-local* part.

Following statements (I)–(III) above, we conclude that comparison of the K & M asymptotic predictions with the standard and improved thin-tube numerical schemes will (i) quantify the large local errors of the original thin-tube model and (ii) exhibit the errors involved in the K & M-type linearization of the finite part of the Biot–Savart integral. We emphasize that the computations of this section will all be performed with normalized circulation $\Gamma = 4\pi$ and for an expansion parameter $\epsilon^2 = 0.25$. This value of ϵ was used in most of the numerical solutions of the asymptotic filament equation (2.12) in the studies by Klein & Majda (1991*b*, 1993) and Klein *et al.* (1992). The favourable comparison with the improved thin-tube model will demonstrate that the asymptotics provide useful insight into the filament dynamics at quite realistic values of the core size parameter $\delta \approx 0.01$–0.02.

Section 5.1 provides some important details regarding how the comparisons in the subsequent sections are built. Mutual tests of numerical and asymptotic predictions of propagation velocity based on a fixed filament geometry are discussed in §5.2. These static tests use a plane sinusoidal distortion of slender vortices in the K & M regime. In §5.3, we consider the temporal evolution of vortex filaments starting from the plane curve initial geometries from §5.2.

5.1. *The basis for comparisons*

Going back to the asymptotic predictions of the filament velocity in (3.22) (and recalling that the specific value of the integral matching parameter ρ is irrelevant) we conclude that the scalar quantity

$$\ln(1/\delta)+C$$

characterizes completely the influence of vortex core size and vortex core structure on the filament motion. In all of the comparisons between asymptotic and numerical predictions which are presented in this section, we will assume that there is a fixed physical reference vortex structure, so that

$$\ln(1/\delta)+C = 1/\epsilon^2-\ln(2\epsilon) = \text{const.} \tag{5.1}$$

This is equivalent to fixing the K & M expansion parameter ϵ; we choose $\epsilon^2 = 0.25$ throughout this section. Given a typical value for the core coefficient of $C = -0.558$, relevant for a Gaussian axial vorticity distribution and zero axial flow, this choice of ϵ corresponds to $\delta \approx 0.01$. This is quite a realistic value comparable, for example, to the core size to wing span ratio for the trailing vortices of a mid-size airplane according to Vitting (1991).

We intend to compare asymptotic predictions with results from the thin-tube vortex element models. In particular, we wish to test the influence of the numerical vorticity smoothing function on the results. We have shown in §4 that any choice of a smoothing function directly corresponds to a (frozen) leading-order axisymmetric (numerical) vortex core structure. Now we are interested in how accurately a thin-tube model with a given smoothing function simulates the evolution of a physical vortex that has the same structure at leading order. Specifically, we want to compare the numerical results with those corresponding to the physical reference vortex introduced above. As a consequence, we have to introduce a relation between numerical core size and the vorticity smoothing function; we let

$$\ln(1/\delta_{g/s}^{ltm})+C_{g/s} = 1/\epsilon^2-\ln(2\epsilon), \tag{5.2}$$

where the subscripts indicate the choice of the third-order Gaussian or the sech^2 smoothing functions

$$f(r) = \frac{3}{4\pi}e^{-r^3} \quad \text{and} \quad f(r) = \frac{3}{4\pi}\operatorname{sech}^2(r^3), \tag{5.3}$$

respectively (see Beale & Majda 1985). The core coefficients $C_g = -0.3212$ and $C_s = -0.2201$ are obtained by evaluating the quadratically nonlinear functional from (3.33) assuming zero axial flow, i.e. $w^{(0)} \equiv 0$, and using the circumferential velocity corresponding to the numerical core structure from (4.22), (4.23). (Notice that the leading-order axial vorticity and circumferential velocity are related via $\bar{r}\zeta^{(0)} = (\bar{r}v^{(0)})_{\bar{r}}$.)

We emphasize that the choice of the numerical core size from (5.2) is the physically correct one. With this choice, the leading-order vorticity distributions and core sizes of the physical reference vortex and its numerical counterpart coincide.

5.2. *Static tests*

The analytical considerations given in §§2–4 are of static nature. They involve asymptotic evaluations of spatial integrals and an asymptotic solution of the leading- and first-order vorticity transport equations, which do not include unsteady terms. Hence, given a fixed filament geometry, it is only natural to compare filament velocity

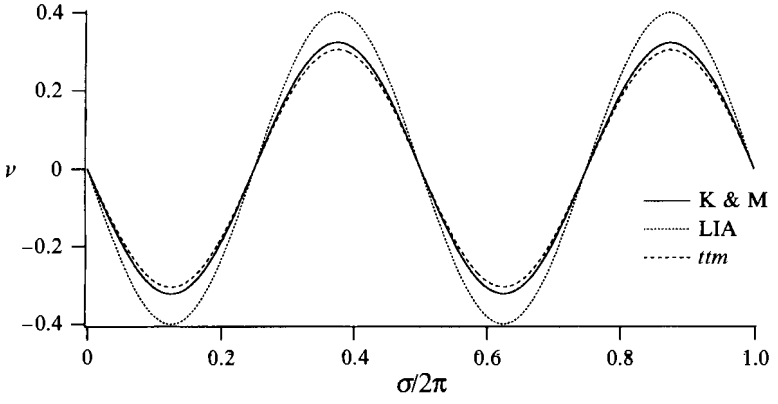

FIGURE 4. Filament velocity predictions for the sinusoidal plane curve geometry from (5.4) with $\epsilon^2 \approx 0.25$ and $\tilde{a} = 0.025$.

predictions from the several different approaches of §§2–4. Such a static comparison has the advantage that errors induced by a specific temporal discretization cannot skew the results.

Here we analyse plane curve sinusoidal geometries described by

$$\boldsymbol{X}(s) = s\boldsymbol{t}_0 + \epsilon^2 \tilde{a} \sin(2s/\epsilon)\, \boldsymbol{n}_0, \tag{5.4}$$

where the amplitude $\tilde{a}$ is to be varied and $\boldsymbol{t}_0$ and $\boldsymbol{n}_0$ are mutually orthogonal unit vectors. Equation (5.4) describes a filament whose reference line lies in the $(\boldsymbol{t}_0, \boldsymbol{n}_0)$-plane. A straightforward symmetry consideration shows that the filament velocity points along the direction of $\boldsymbol{b}_0 = \boldsymbol{t}_0 \times \boldsymbol{n}_0$, i.e. it is everywhere normal to the $(\boldsymbol{t}_0, \boldsymbol{n}_0)$-plane. Thus, it is sufficient to display only one scalar quantity in the following comparison: the filament velocity in the direction of $\boldsymbol{b}_0$. The theoretical prediction for this velocity component from (2.6), (2.9) is

$$v^{K\&M}(\sigma) = -\frac{4\tilde{a}\sin(2\sigma)}{[1+\epsilon^2\tilde{a}^2\cos^2(2\sigma)]^{3/2}} - \epsilon^2\tilde{a}\hat{\mathrm{I}}(2)\sin(2\sigma), \tag{5.5}$$

where $\sigma \equiv s/\epsilon$ and $\hat{\mathrm{I}}(\cdot)$ is the Fourier-symbol of the I-operator in (2.10), (2.11). This prediction will be compared below with the output from the standard and improved thin-tube models of §4.

Improvement of the thin-tube model

Here we demonstrate the quantitative improvement that is achieved by the local corrections to the standard thin-tube model discussed in §4. Figures 4 and 5 show results for the plane curve geometry from (5.4) with $\tilde{a} = 0.1$. Figure 4 includes filament velocity predictions from the local induction approximation (LIA) (see Batchelor 1967 or Hasimoto 1972), the Klein & Majda (1991*a*, *b*) asymptotics and the spectral version of the standard thin-tube model described in §4. We observe a 25–30% deviation between the local induction approximation and the asymptotic prediction. This underscores the conclusion by Klein & Majda (1991*a*) that in the present regime of perturbed slender vortices, the local induction approximation does not provide a valid description of the filament dynamics. Between the K & M theory and the standard thin-tube model we still find deviations of about 7% in the present case. For the small value of $\tilde{a} = 0.1$ considered, these differences are dominated by the erroneous prediction of

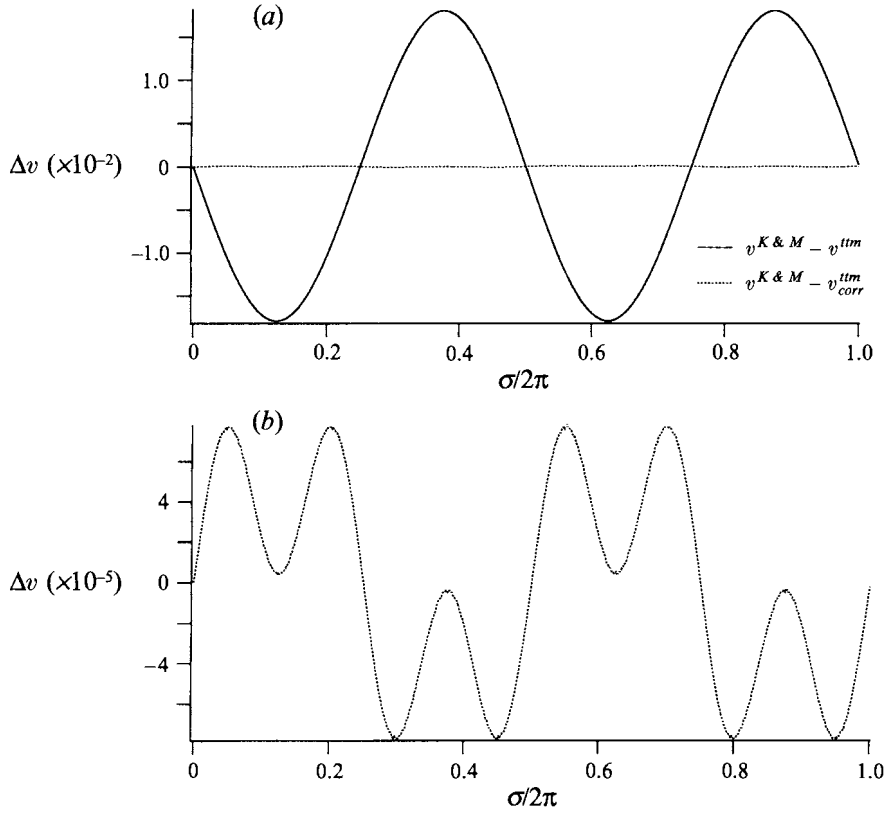

FIGURE 5. Deviations between the theoretical and numerical filament velocity predictions for the configuration of figure 4. (*a*) Comparison of the K & M theory to the standard and improved thin-tube models, (*b*) comparison of the K & M theory to the improved thin-tube scheme on an appropriate scale.

local effects in the numerical method. We infer this from figure 5(*a*) which shows the differences between K & M and the standard thin-tube scheme (solid line) and between the K & M theory and one of the corrected thin-tube models of §3 (dashed line). We find that the local correction effectively removes the discrepancy between the asymptotic and numerical predictions. In fact, the scaled velocity difference $|v^{K\&M} - v^{ttm}|/\kappa$ varies about its average of 0.199 by no more than 2%, so that a local correction proportional to the curvature κ yields the desired result. Which particular version of the corrections in §4 we choose for this comparison is practically irrelevant. The predicted filament velocities from all the corrected schemes differ only in the sixth relevant digit.

In figure 5.2(*b*) we display the velocity difference $(v^{K\&M} - v^{ttm}_{corr})$ between the asymptotic and the corrected numerical predictions on an appropriate blown-up scale. The maximum deviation is less than 10^{-4}, i.e. it is less than about 0.3‰ of the maximum filament velocity from figure 4. We observe that this remaining deviation has a distinctive spatial structure that is dominated by two sinusoidal contributions with wavenumbers $\xi = 2$ and 6. In fact, Fourier analysis of the graph in figure 5(*b*) shows that the amplitudes of all other modes are smaller by at least a factor of $\frac{1}{100}$ than those of modes 2 and 6. We recall from the preceding discussion that deviations between the asymptotic and numerical predictions can be due to errors in either the local or non-

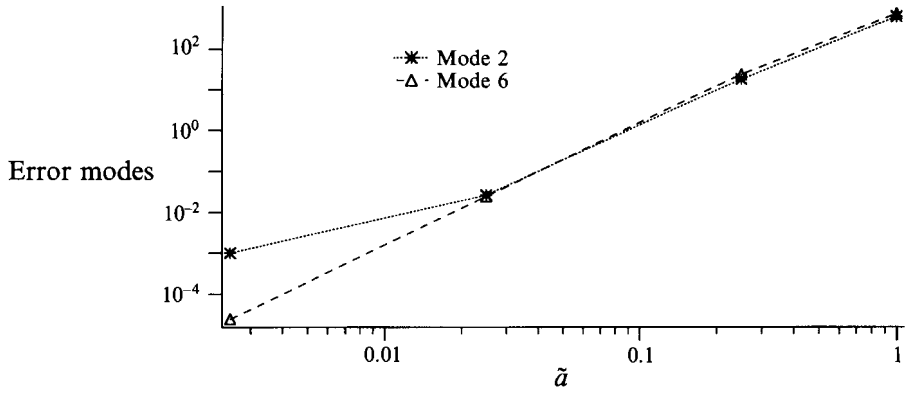

FIGURE 6. Scaling of the Fourier modes with wavenumbers 2 and 6 of the deviation between the predictions from the K & M theory and from the improved thin-tube model.

local contributions to the filament velocity. Local errors must inherit the periodicity features of the curve geometry, so that only the mode-2 contribution to the deviations in figure 5(*b*) can be of local nature. As a consequence, the mode-6 deviation reflects the error of the K & M linearization of the finite part of the Biot–Savart integral in (2.9), (2.10).

Validity of the Klein–Majda theory

For $\tilde{a} = 0.1$ the effective amplitude–wavelength ratio of the filament geometry from (5.4) is $0.1/4\pi \approx 8 \times 10^{-3}$ and, as expected, the linearization of the Biot–Savart integral provides a very good approximation. Next, we investigate the scaling of the deviations between the K & M theory and the corrected thin-tube model as the amplitude, $\tilde{a}$, of the sinusoidal displacement varies. To this end, we consider the sequence of amplitudes $\tilde{a} = 0.01$, 0.1, 1.0 and 4.0 and Fourier-analyse the velocity difference $(v^{K\&M} - v^{ttm}_{corr})$. Figure 6 shows, in a double-logarithmic representation, the dependence of the mode-2 and mode-6 amplitudes of this deviation as a function of $\tilde{a}$. For mode-6 the amplitude scales precisely with the third power of $\tilde{a}$. For mode-2 this is true at larger values of the amplitude, while for $\tilde{a} = 0.01$ a deviation from the third-power scaling occurs. We conjecture that this deviation is due to the fact that mode-2 includes both local and non-local errors, and that the results are affected by discretization errors which are small, but scale with less than the third power of $\tilde{a}$. These errors become relevant only for very small amplitudes.

For the present class of plane sinusoidal displacements there is an amplitude threshold beyond which the linearization errors from the K & M theory become comparable to our local corrections to the numerical scheme. Figure 7 shows the velocity differences $(v^{K\&M} - v^{ttm})$ and $(v^{K\&M} - v^{tmm}_{corr})$ for $\tilde{a} = 1.0$. We observe that, by using the corrected thin-tube model, one can still remove the largest discrepancies between the standard thin-tube scheme and the theoretical prediction. The remainder is of the same order of magnitude as the local corrections, but in absolute value it is only about 2% of the maximum induced filament velocity. Thus, the theory yields acceptably accurate approximations up to amplitudes $\tilde{a} = 1.0$ for the present plane curve geometry and for the present choice of the expansion parameters $\delta \approx 10^{-2}$ and $\epsilon^2 \approx 0.25$. The comparison of the temporal evolution of filaments with plane curve initial data in the following subsection will include one case with amplitude $\tilde{a} = 1.0$. As shown below, the convincing agreement between theory and numerical predictions

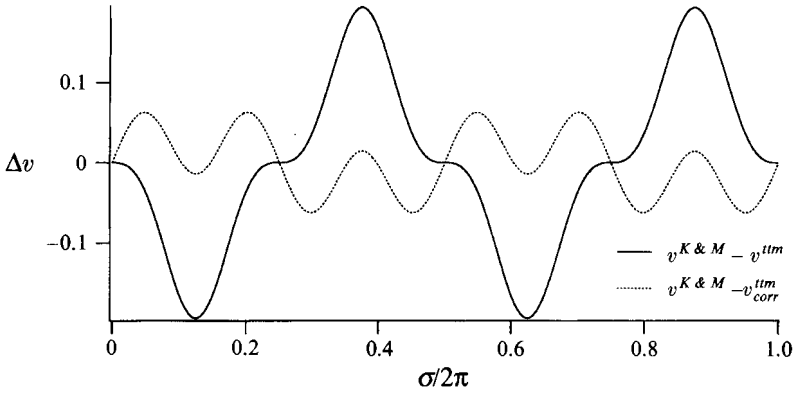

FIGURE 7. Deviations between the theoretical and numerical filament velocity predictions for the sinusoidal plane curve geometry from (5.4) with $\epsilon^2 \approx 0.25$ and $\tilde{a} = 1.0$: comparison of the K & M theory with the standard and improved thin-tube models.

achieved in this example can also be observed in unsteady experiments, showing that the dynamical evolution of the slender filament is also appropriately captured by the asymptotic theory at the border of its validity.

5.3. *Comparison of dynamic predictions*

In this section we consider the temporal evolution of slender vortices with plane curve initial perturbations of the filament reference lines. First we use the sinusoidal distortions from the previous section to demonstrate that the K & M asymptotics and corrected thin-tube predictions are in much closer agreement than theory and uncorrected thin-tube model. We then use more general initial data for an extensive comparison of numerical and theoretical predictions including, in particular, one set of initial data that is formally outside the regime of validity of the asymptotics.

All the results in this section are based on a spatial resolution of 1024 nodes in the thin-tube vortex element computations and 512 gridpoints in the evaluations of the asymptotic filament equation from (2.12). We emphasize that, except for the third example with initial data from (5.9*b*) below, this is almost an overkill of resolution for the asymptotics and that practically equivalent results can be obtained even with 128 gridpoints.

An important aspect of the present comparisons concerns the time scaling. The asymptotic theory involves several time rescalings and a special choice of spatial coordinates suitable for an efficient numerical implementation. For a successful quantitative comparison, these factors have to be appropriately accounted for. We summarize the space–time rescalings used in our computations in Appendix B. The transformations given there are used to map thin-tube model results into the coordinate system constructed in the asymptotic theory. Dynamic predictions are compared in the corresponding space–time system, unlike the static comparison experiments which have been conducted above in normalized physical space.

Sinusoidal plane curve distortions

Here we consider the plane curve initial data from (5.4) with $\tilde{a} = 1.0$. Figure 8(*a*) shows the time evolution of the maximum curvature of the filament reference line. The time variable in the graph is the Klein–Majda time coordinate, τ, from (2.8). As mentioned above, there is qualitative agreement between all three prediction methods – the K & M asymptotics, the standard thin-tube model and the improved numerical

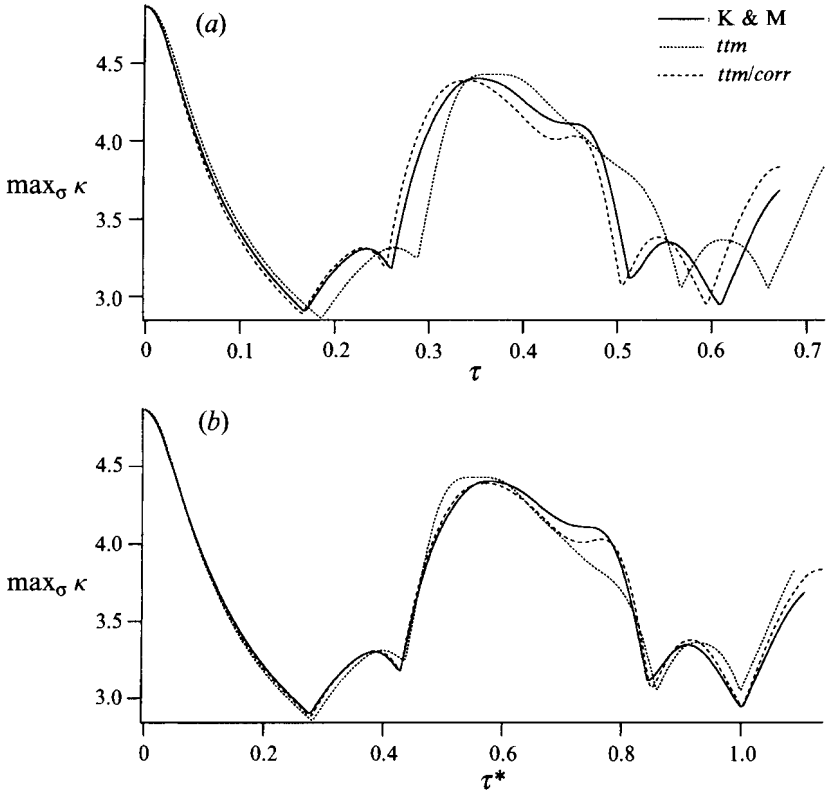

FIGURE 8. Time histories of the maximum curvature in the computational domain based on the asymptotic and standard and corrected thin-tube predictions for the sinusoidal plane curve initial data from (5.4) with $\tilde{a} = 1.0$: (*a*) direct output from numerical computations, (*b*) comparison with individually rescaled time variables so as to remove a systematic timescaling error.

scheme from §4.2. The differences between the curves may be attributed to two distinct effects. One is a systematic time delay, the other is the net deviation between the curves after deletion of this time delay through a suitable time rescaling. To separate the two effects, we display in figure 8(*b*) the same data as in figure 8(*a*), but with an individual time rescaling applied to each curve, so that the last local minima (around $\tau = 0.6$) coincide in the rescaled time. Thus, for each graph we define a related time variable

$$\tau_I^* = \tau/\tau_I^{ref}, \tag{5.6}$$

where I replaces one of $K\&M$, *ttm*, or *ttm, corr* and where τ_I^{ref} is the time at which the last local minimum occurs on the K & M curve in figure 8(*a*). From the graphs of figure 8(*b*) it becomes even more apparent that the K & M asymptotic and corrected thin-tube predictions practically coincide, whereas there is a considerable deviation for the standard thin-tube model. Notice that the additional time rescaling applied here is purely *ad hoc* and, in contrast to the derivations in Appendix B, does not reflect a systematic scale transformation obtained by analytic considerations. The transformation from figure 8(*a*) to 8(*b*) just emphasizes the fact that two types of deviations between the different predictions occur: a time delay and a shape error.

Figure 9(*a*, *b*) demonstrates that there is also close agreement between the theoretical and corrected numerical results in the spatial solution structure. The graphs include the spatial distribution of the filament curvature at the output times $\tau = 0.3968$ (*a*) and $\tau = 0.5284$ (*b*) for the corrected thin-tube computation. These results are compared with

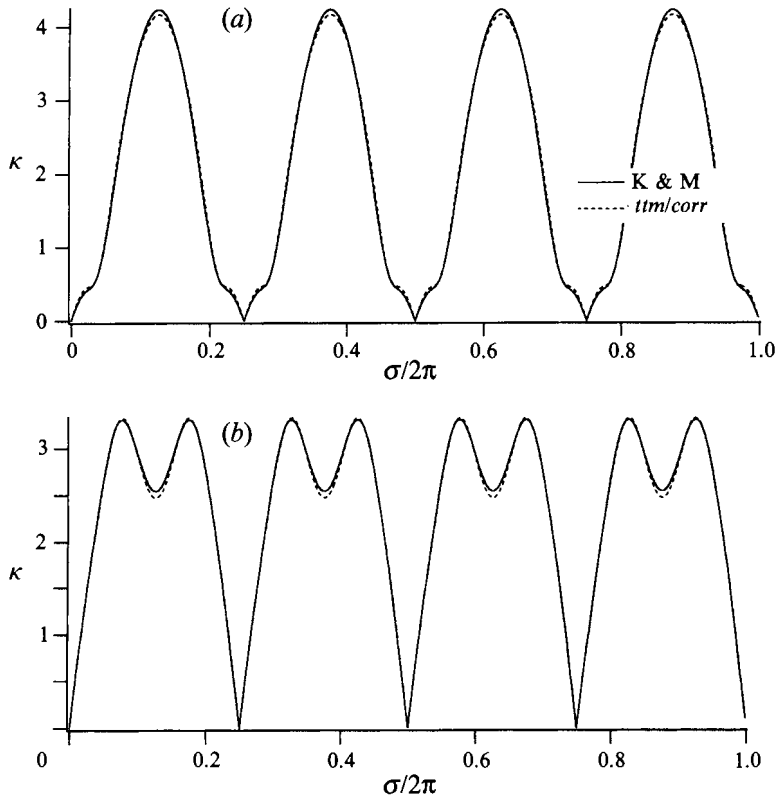

FIGURE 9. Spatial curvature distributions from asymptotic theory (K & M) and from the corrected thin-tube computations (*ttm, corr*) for the same initial data used to generate figure 8 at two output times chosen for equal values of τ_I^* ($I = K\&M$ or *ttm/corr*) from (5.6): (*a*) $\tau = 0.3968$ (*ttm/corr*), $\tau = 0.4062$ (K & M); (*b*) $\tau = 0.5284$ (*ttm/corr*), $\tau = 0.5409$ (K & M).

the K & M asymptotic predictions for equal values of the τ_I^*. The associated output times for the asymptotic computation are $\tau = 0.4062$ (*a*) and $\tau = 0.5409$ (*b*). The very close agreement is obvious; the largest relative difference between the two curvature distributions in figure 9(*a*), when scaled with the maximum curvature from this plot, is no more than 1.6%.

Klein & Majda (1991*a*, *b*) emphasize that their asymptotic theory includes the (non-local) effects of vortex self-stretching. The quadratically nonlinear functional

$$\frac{1}{l}\dot{l}(\sigma,\tau) = \epsilon^2\frac{1}{4}\int_{-\infty}^{\infty}\frac{1}{|h|}[\bar{\psi}(\sigma+h,\tau)\,\psi(\sigma,\tau)-\bar{\psi}(\sigma,\tau)\,\psi(\sigma+h,\tau)]\,\mathrm{d}h \tag{5.7}$$

of the filament function from (2.13) describes the local rate of self-stretching with relative errors of $O(\epsilon)$, given the exact filament function. In thin-tube simulations, the extension of individual vortex elements is used as a direct measure for the local rates of stretching. In the straight-segment approximation, the stretching of the elements is approximated as

$$\left(\frac{1}{l}\dot{l}\right)_{i+1/2} \approx \frac{1}{|\chi_{i+1}-\chi_i|}\frac{\mathrm{d}}{\mathrm{d}t}|\chi_{i+1}-\chi_i| \tag{5.8a}$$

while

$$\left(\frac{1}{l}\dot{l}\right)_i \approx \frac{1}{|\delta\chi_i|}\frac{\mathrm{d}}{\mathrm{d}t}|\delta\chi_i| \tag{5.8b}$$

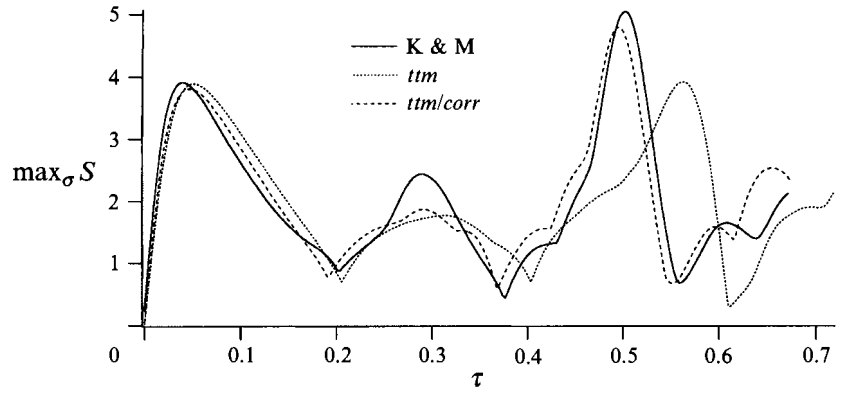

FIGURE 10. Time histories of the maximum local stretching rate in the computational domain based on the asymptotic and standard and corrected thin-tube predictions for the sinusoidal plane curve initial data from (5.4) with $\tilde{a} = 1.0$.

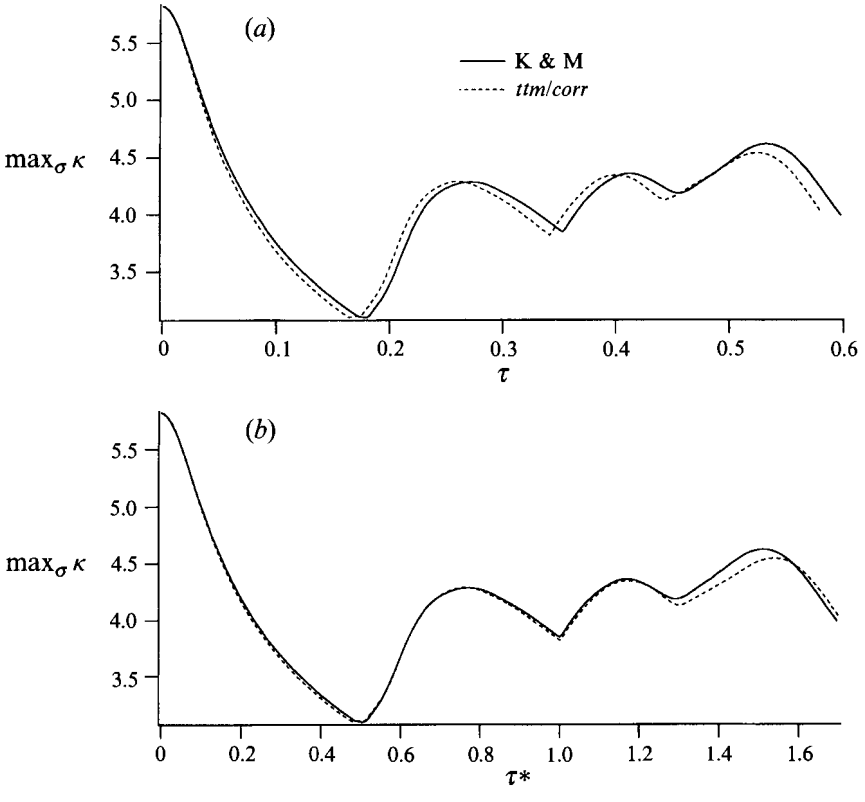

FIGURE 11. Time histories of the maximum curvature in the computational domain based on the asymptotic and standard and corrected thin-tube predictions for the two-mode plane curve initial data from (5.9*a*): (*a*) direct output from numerical computations; (*b*) comparison with individually rescaled time variables so as to remove a systematic timescaling error.

is used in conjection with spectral representation. In figure 10 we compare the time histories of the maximum local stretching rate in the domain of integration obtained via asymptotic theory, and the standard and corrected thin-tube computations. There is still qualitative agreement and, in particular, the structure of the third hump of the

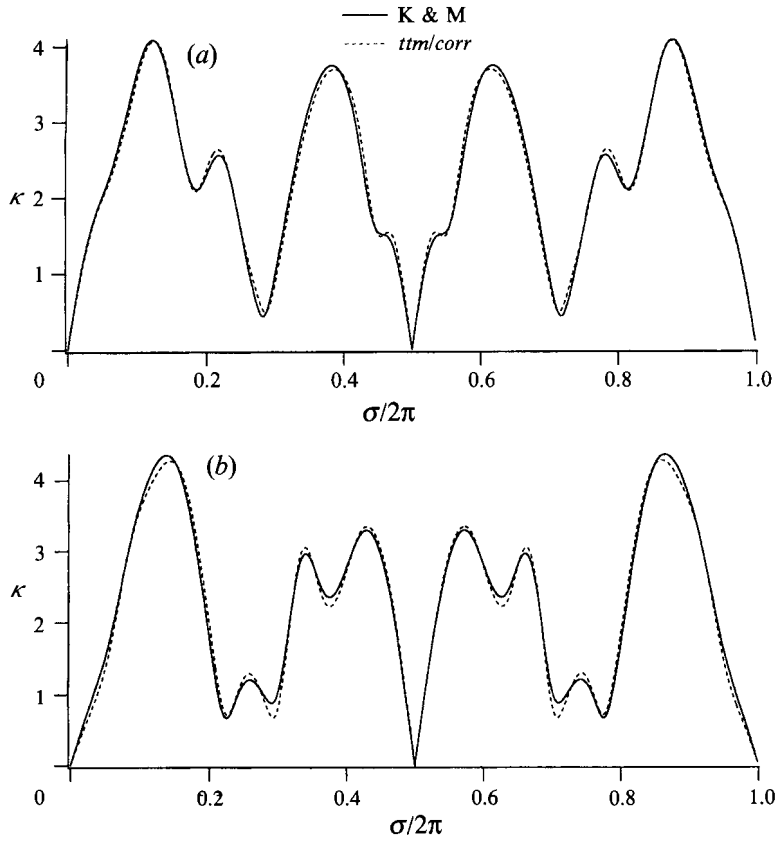

FIGURE 12. Spatial curvature distributions from asymptotic theory (K & M) and from the corrected thin-tube computations (*ttm/corr*) for the same initial data used to generate figure 11 at two output times chosen for equal values of τ_I^* ($I = K\&M$, *ttm/corr*) from (5.6): (*a*) $\tau = 0.3598$ (*ttm/corr*), $\tau = 0.3719$ (K & M); (*b*) $\tau = 0.4716$ (*ttm/corr*), $\tau = 0.4874$ (K & M).

curves is very similar in the asymptotic and corrected numerical result. However, the agreement is not as good as that established for the maximum curvature histories from figure 8. One reason for this may be the fact that only one linearization is involved in producing the curvature histories asymptotically, while two consecutive linearizations are applied in generating the stretch rate histories: in going from the original filament equations of motion to the Klein–Majda filament equation with self-stretch from (2.12) one has to linearize the finite part of the Biot–Savart integral. Using the resulting filament function to generate the stretch rate distributions according to (5.7) involves another linearization that is explained in detail by Klein & Majda (1991*b*). Hence one can expect larger deviations between the asymptotics and the corrected thin-tube stretching rate predictions than were observed for the curvature histories.

Two-mode plane curve displacements

Here we consider filament reference line initial data of the form

$$\boldsymbol{X}(s) = s\boldsymbol{t}_0 + \epsilon^2[\sin(s/\epsilon) + \sin(2s/\epsilon)]\,\boldsymbol{n}_0 \tag{5.9a}$$

and

$$\boldsymbol{X}(s) = s\boldsymbol{t}_0 + \epsilon^2[\sin(2s/\epsilon) + \sin(3s/\epsilon)]\,\boldsymbol{n}_0, \tag{5.9b}$$

and again we let $\epsilon^2 = 0.25$. Figure 11(*a*, *b*) displays the time history of the maximum

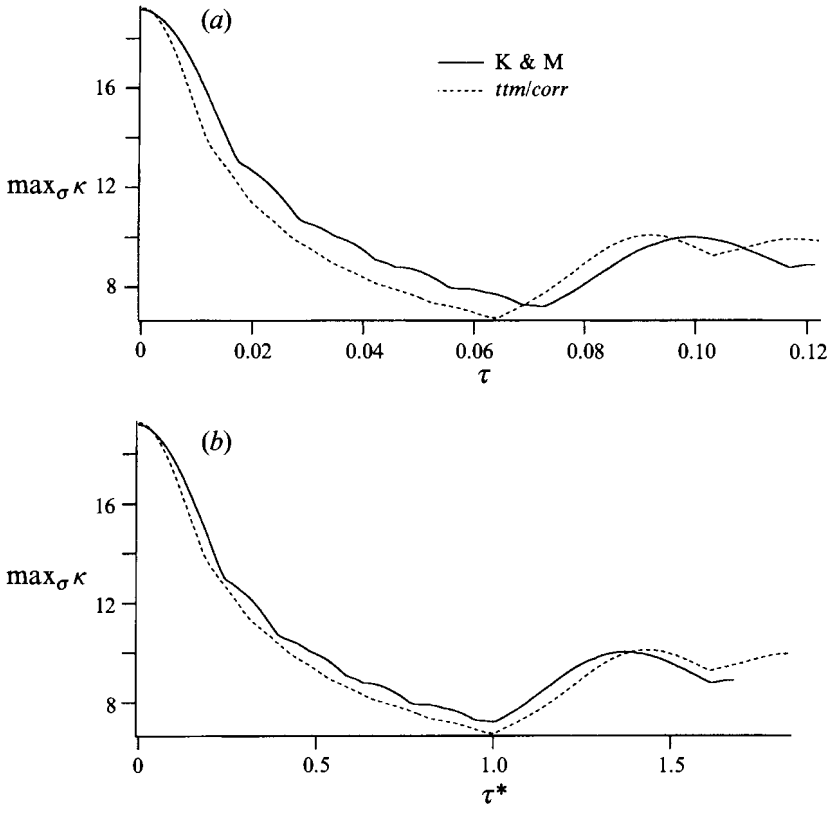

FIGURE 13. Time histories of the maximum curvature in the computational domain based on the asymptotic and standard and corrected thin-tube predictions for the two-mode plane curve initial data from (5.9*b*): (*a*) direct output from numerical computations, (*b*) comparison with individually rescaled time variables so as to remove a systematic timescaling error.

curvature for the initial data from (5.9*a*) as obtained from the asymptotics and from the corrected thin-tube model computation. As in figure 8 the first graph compares the direct output from the computational codes, while figure 11(*b*) shows the same curves after an individual time rescaling similar to that described in (5.6) above. Here we have used the time for the appearance of the second local minimum of the curvature histories as a reference time. The agreement is again very satisfactory. Figure 12(*a*, *b*) shows comparisons of spatial curvature distributions at output times $\tau = 0.3598$ (*a*) and $\tau = 0.4716$ (*b*) for the corrected thin-tube computation. For equal values of the τ_I^* this corresponds to output times $\tau = 0.3719$ and $\tau = 0.4874$, respectively, in the K & M asymptotics. Again the agreement between theory and computation is quite convincing, even though the maximum curvature is now in the range of $\kappa = 4.5$ during most of the computation. With the geometry expansion parameter as large as $\epsilon^2 = 0.25$, this is at the border of validity of the asymptotics.

The initial data from (5.9*b*) represent a severe test for the asymptotic theory, because the maximum initial curvature is $\max_\sigma \kappa(\sigma, 0) \approx 19.0$. Considering that this value is larger than $1/\epsilon^2$ by a factor of about five, we find that this example should be outside the regime of validity of the asymptotics. Agreement between asymptotic and numerical predictions may therefore be expected to be at most qualitative, and this is what we in fact observe. Figure 13(*a*, *b*) displays the time history of the maximum curvature in the same way as discussed earlier. Again we find qualitative agreement

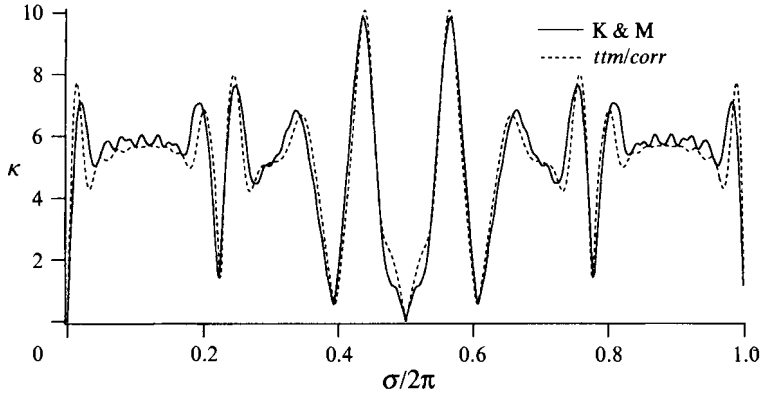

FIGURE 14. Spatial curvature distributions from asymptotic theory (K & M) and from the corrected thin-tube computations (*ttm/corr*) for the initial data from figure 13 at an output time chosen for equal values of τ_I^* ($I = K\&M, ttm/corr$) from (5.6): $\tau = 0.09341$ (*ttm/corr*), $\tau = 0.1055$ (K & M).

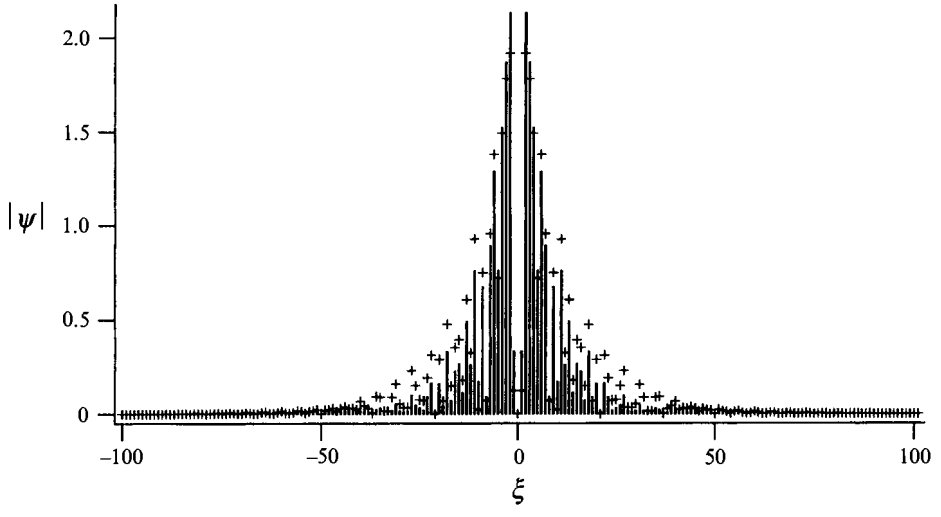

FIGURE 15. Fourier spectra of the filament function in the computation of figures 13 and 14, for the initial data and at time $\tau = 0.1055$.

between asymptotic theory and thin-tube model results. The principal difference between the curves is that the theoretical prediction involves a much rougher development of the curvature maximum, with pronounced kinks in the graph. These are smoothed out in the curvature history from the corrected thin-tube model. We conjecture that the rougher solution structure from the theory is due to the neglect of nonlinear contributions to the finite part of the Biot–Savart integral which are accounted for correctly in the numerical scheme and which may have an important dispersive effect.

Figure 14 shows the spatial curvature distributions for equal τ_I^* corresponding to $\tau = 0.09341$ in the numerical computation and $\tau = 0.1055$ in the numerical solution of the filament equation. We also observe a qualitative agreement and that the small-scale structure of the K & M asymptotic solution is much rougher than that of the thin-tube model prediction. To elucidate this point in more detail, we display in figure 15 the Fourier spectra of the filament function at times $\tau = 0.0$ (+) and $\tau = 0.1055$ (lines from

zero), the latter corresponding to the output time in figure 14. At time zero the spectrum includes non-zero contributions at wavenumbers larger than $\xi = 50$, which is roughly the wavenumber associated with the vortex core diameter for $\epsilon^2 = 0.25$ according to Klein & Majda (1991*b*). Notice that a smooth Fourier spectrum for the filament function occurs in these cases, even though the geometrical initial data involve only one or two discrete modes. This is due to the transformation from the straight-line coordinate in the description of the initial geometry to the arclength variable required in the implementation of the Hasimoto transformation.

Since the asymptotic theory is based on the assumption that the characteristic wavelengths for the filament function are long compared to the vortex core size, it is clear that the current example strongly stresses the applicability of the analysis. An interesting observation is that at the later time (lines from zero) the spectrum has narrowed, so that apparently the Fourier modes with wavenumbers larger than the core size scale are damped in the evolution under the filament equation. This shows that the asymptotic theory is robust in the sense that initial data outside the regime of validity of the asymptotics are automatically driven back into the correct range. We remind the reader that Klein & Majda (1991*b*) show by explicit examples that in the wavenumber range below the core size scale, $0 \leqslant \xi \leqslant \xi_{core} \approx 50$, there is an energy transfer from long to short waves, which appears to be reversed outside of this range of wavenumbers following the present results.

In conclusion we find that

(i) the local corrections to the standard thin-tube model yield good agreement between numerical and asymptotic predictions in dynamical computations even in a regime close to the border of validity of the asymptotic theory;

(ii) even well outside the formal regime of validity the asymptotic theory yields satisfactory qualitative insights into the filament dynamics.

In addition, we emphasize that the present results exhibit clearly the power of asymptotic analysis. The thin-tube model computations of this section require roughly on the order of one CPU hour on a CRAY C90 each, while the solutions to the asymptotic filament equation have been generated within minutes on a MacIntosh IIci desktop computer or within seconds on an HP 9000 series workstation. Computational difficulties associated with thin-tube modelling are discussed in more detail in the following section.

6. Discussion

In this section, we discuss the key issues of the asymptotic treatment of the vorticity transport equation and the resulting insight which, in particular, led to the formulation and construction of the corrected thin-tube models of §3.

6.1. *Slender cores and the asymptotic treatment of the vorticity transport equation*

Despite its simplicity, the notion of a 'slender vortex with leading-order axisymmetric core structure' is not as intuitive as it appears. One potential source of difficulty, which had to be overcome during the course of this effort, stems from the fact that in a large number of situations one is given (or would like to assign) a complete description of the core vorticity distribution. This is the case for the thin-tube *model*, which 'inherits' – by 'butchering' its parent, the vortex element *method* – a core vorticity distribution whose shape is dictated by the choice of core smoothing function. Since, as in the vortex element method, it is emphasized that the standard thin-tube model relies on exact evaluation of the line Biot–Savart integral over the discretized smooth vorticity

field, it is only natural to wonder, for example, why is it that a 'correction' is needed at all? From a purely mathematical point of view, the need for correction of the filament propagation velocity predicted by the standard thin tube model can be motivated and justified on the basis of the construction itself. Below, we first summarize this construction and then return to address the question at hand based on the insight gained from this exercise.

Construction of velocity corrections

The theoretical foundation of the improved thin-tube model presented here is the new asymptotic analysis of the vorticity structure of slender vortices as described in §§2 and 3, which summarizes the calculations by Klein (1994) and Klein *et al.* (1994). In a first step this analysis shows that the filament velocity is identical to the induced velocity on a certain curve, called the connecting line of stagnation points, that is located within an $O(\delta^2)$ vicinity of the vortex centre. This induced velocity is shown to consist of a local and a non-local contribution, i.e.

$$\boldsymbol{X}_t = C_\delta \kappa \boldsymbol{b} + \boldsymbol{Q}_f. \tag{6.1}$$

The non-local finite part of the line Biot–Savart integral, $\boldsymbol{Q}_f$, depends solely on the overall circulation, Γ, of the vortex and on the instantaneous filament geometry. The local part is proportional to the product $\kappa \boldsymbol{b}$ of the curvature and the local binormal unit vector. The factor of proportionality is

$$C_\delta = \ln(2/\delta) + C, \tag{6.2}$$

where $\ln(2/\delta)$ is a scaling contribution determined by the characteristic diameter δ of the vortex core and C is the linear functional of the leading- and first-order axial vorticities $\zeta^{(0)}$ and $\zeta_{11}^{(1)}$ from (3.23).

These formulae for the filament velocity are the direct result of a suitable asymptotic evaluation of the Biot–Savart integral applied to a vector field $\boldsymbol{\omega}$ that is concentrated along a smooth space curve and is to leading-order axisymmetric with respect to this reference curve. This vector field may or not satisfy the vorticity transport equation, but if it does, we have the relevant results describing the motion of a slender vortex. The key observation leading to our proposed improvement of the thin-tube model is that the vortex element node velocities in the standard scheme are obtained precisely by doing just that, namely by evaluating the Biot–Savart integral at the nodes, based on the *numerical* vorticity distribution $\boldsymbol{\omega}^{ttm}$ from (4.1).

An asymptotic analysis for small δ of this vector field uniquely identifies the numerical leading-order axisymmetric vorticity $\zeta^{(0),ttm}(\bar{r})$ in terms of the vorticity smoothing function f_δ from (4.4), (5.3). Similarly it provides the numerical first-order vorticity component $\zeta_{11}^{(1),ttm}(\bar{r})$. Thus, all the formulae for the filament velocity cited above apply and yield an explicit asymptotic representation of the numerical node velocity that can be compared directly with the physically correct expressions.

Since $\boldsymbol{Q}_f$ depends only on the overall circulation and on the filament geometry, this part of the filament velocity is handled with high accuracy by the numerical scheme. Two errors arise in the local part, both of which are responsible for leading-order deviations from the physically correct filament velocity. The first error is that the vortex element nodes do not lie on the connecting line of stagnation points within the *numerical* vortex core. The second error is due to a false prediction of the first-order vorticity mode $\zeta_{11}^{(1)}$ in the numerical scheme. In fact, the physical $\zeta_{11}^{(1)}(r)$ is determined by a balance of convection and vortex stretching in the filament core, while the numerical mode $\zeta_{11}^{(1),ttm}(\bar{r})$ is due solely to the geometrical deformation of the

overlapping vortex elements as shown in §4. Thus, $\zeta_{11}^{(1),ttm}(\bar{r}) \neq \zeta_{11}^{(1)}(\bar{r})$, even if one can achieve agreement between $\zeta^{(0),ttm}(\bar{r})$ and $\zeta^{(0)}(\bar{r})$ through a suitable choice of the numerical vorticity smoothing function.

Having identified these error sources, we are able to suggest three different modifications of the standard thin-tube model that are not equivalent, but all reduce the leading-order errors discussed above down to $O(\delta)$.

(i) *Velocity corrections.* By comparison of the asymptotic formulae (6.1), (6.2), (3.23), (3.21; with $\rho \equiv 1$) for the local induced velocities when applied to the physical and numerical vorticity structures, determine a velocity defect. Add this defect velocity to the induced node velocities from the standard thin-tube model.

(ii) *Node corrections.* Determine the location of the local stagnation point in the numerical vortex core closest to a vortex element node and evaluate the Biot–Savart integral at this corrected location. Then move the node at this velocity.

(iii) *Rescaled standard model.* Observe that the only relevant quantity carrying the vortex core structure information is $\ln(2/\delta)+C$ or equivalently, the parameter ϵ defined by

$$\epsilon^2 = [\ln(2\epsilon/\delta)+C]^{-1}, \tag{6.3}$$

which also appears as the relevant expansion parameter in the Klein–Majda asymptotics discussed in §2. Given the correct physical value of C and of C^{ttm} as computed from the numerical leading- and first-order vorticities according to (3.23), adjust the numerical core size parameter in such a way that

$$\ln(2/\delta)+C = \ln(2/\delta^{ttm})+C^{ttm} \quad \text{or} \quad \delta^{ttm} = \delta\exp(C^{ttm}-C). \tag{6.4}$$

Then run the standard thin-tube model with the asymptotically rescaled numerical vortex core size.

Versions (i) and (ii) require discrete computations of the filament curvature and of the local normal and binormal vectors, while version (iii) just involves a rescaling of the parameters, but no modification to the computational code. Therefore, version (iii) is the easiest to implement and the most elegant, but its application requires a very careful consideration and distinction between numerical and physical core structures and core sizes.

The need for velocity corrections

As can be appreciated from the summary provided above, the predictions of the standard thin-tube model must be corrected because the model formulation in fact assumes 'too much'. On one hand, the construction of the thin-tube model yields a frozen (time-independent) leading-order axisymmetric vorticity distribution. It has been shown by Callegari & Ting (1978) that the core structure is generally time dependent, and by Klein & Ting (1992) that the filament asymptotics even allows for axial variations of the core structure (see also Ting & Klein 1991). Only in very special regimes, such as that considered by Klein & Majda (1991*a*, *b*) and in this paper, is it true that the core structure may be considered constant in space and time on the relevant timescales. In the standard thin-tube model, one further assumes that the node locations used in the formulations coincide with the local relative core stagnation point. By doing so, one implicitly assumes that the first-order vorticity distribution at the node location is consistent with the prevailing leading-order numerical vorticity

distribution and with the vorticity transport equation. Unfortunately, the asymptotic analyses of both the quasi-steady vorticity transport equation and the numerical vorticity distribution reveal, by direct computation, that this is not the case. In other words, the thin-tube first-order vorticity distribution which one also inherits in the course of the numerical construction is not consistent with the assumption that the node coincides with the local relative stagnation point. Consequently, the velocity predictions must somehow be corrected.

A key element in our construction and implementation of thin-tube velocity corrections is our ability to fully characterize the leading- and first-order core numerical vorticity distributions and to compare directly with an asymptotic treatment which is based on the same quantities. Thus, we are able to formulate three different corrections strategies: (*a*) explicit velocity corrections, (*b*) node–stagnation point corrections, and (*c*) re-scaled core radius. In implementing the first and second corrections, it is natural to identify the physical with the numerical leading-order core structure. This is by no means a necessary condition. In fact, one only needs agreement in the effective value of the expansion parameter ϵ in order to obtain correct predictions of the filament velocity, and this insight is at the core of the third correction strategy.

All of the correction strategies shown above achieve, through different means, this desired result. However, it should be noted that assuming the numerical and the physical leading-order vorticity distributions to coincide does not imply that the numerical first-order vorticity distribution is automatically relevant or meaningful as well. Nor does it imply that the node-to-stagnation-point displacement derived above is a physically meaningful quantity. This is not a consequence of any deficiency in the asymptotic analysis but rather due to the fact that the first-order core vorticity distribution of the thin-tube model is a purely numerical entity.

Further interpretations and Fraenkel's analysis of slender vortex rings

It should be emphasized that the first-order vorticity distribution $\zeta_{11}^{(1)}(\bar{r})$ derived during the course of the asymptotic treatment of the vorticity transport equation is defined with respect to the local core stagnation point. In the development of the asymptotic theory, determination of the exact location of this point – with respect to, for example, the filament reference line – is neither necessary nor performed. All that is in fact required is the existence of such a point within an inner $O(\delta^2)$ core surrounding the reference line. Since this 'apparent flexibility' in the asymptotic analysis may be the source of some confusion, it is worthwhile providing further interpretation of the role of the first-order vorticity distribution.

One attractive interpretation is to view the role of the first-order vorticity distribution as fixing the spatial location of the local stagnation point. In other words, if the correct first-order vorticity distribution at the node is specified, then our asymptotic treatment of the vorticity transport equation naturally provides the correct node-to-stagnation-point separation distance. In order to support this statement, we compare our asymptotic predictions of node–stagnation separation distance with those of Fraenkel (1972) who analysed, using a completely different approach, the propagation of steady vortex rings.

In Fraenkel's analysis, thin rings of nearly circular core cross-section are assumed, as well as a 'constant' core vorticity distribution:

$$\omega(\rho) = \omega|_{\bar{r}=0}\,\kappa\rho(\bar{r},\varphi) \quad \text{for} \quad 0 \leqslant \bar{r} = r/\delta \leqslant 1, \tag{6.5}$$

where κ is the curvature of the ring reference line, $\rho(\bar{r},\varphi)$ denotes the distances from the axis of the vortex ring and (r,φ) are the filament-attached radial and circumferential

coordinates as introduced in §3. Using the notation and definitions of the asymptotic analysis, the leading-order vorticity distribution of the slender ring is constant,

$$\varsigma^{(0)} = \Gamma/\pi, \tag{6.6}$$

while the first-order distribution with respect to the core centroid is given by

$$\varsigma^{(1),\,centroid} = -\kappa\varsigma^{(0)}(0)\,\bar{r}\cos\varphi, \quad 0 \leqslant \bar{r} \leqslant 1, \tag{6.7}$$

which immediately gives

$$\varsigma_{11}^{(1),\,centroid} = -k\varsigma^{(0)}(0)\,\bar{r}. \tag{6.8}$$

Associated with the leading-order axisymmetric vorticity distribution of (6.6) is the leading-order axisymmetric velocity field:

$$v_\theta^{(0)}(\bar{r}) = \begin{cases} (\Gamma/2\pi)\,\bar{r}, & 0 \leqslant \bar{r} \leqslant 1 \\ \Gamma/(2\pi\bar{r}), & \bar{r} \geqslant 1. \end{cases} \tag{6.9}$$

Substituting (6.9) into (3.33) and performing the integrals, we obtain the core structure coefficient,

$$C = -\tfrac{1}{4}. \tag{6.10}$$

As expected, this is the same constant that appears in Kelvin's formula for the self-induced propagation velocity of rings of constant vorticity. Meanwhile, inserting (6.6) and (6.8) into (1.8) yields a core structure coefficient,

$$C^{centroid} = 1. \tag{6.11}$$

When appropriately substituted into (4.11), (4.12), the core structure coefficients of (6.10) and (6.11) immediately enable us to estimate the centroid–stagnation point displacement; we have

$$\rho_{stagnation} = \rho_{centroid} + \tfrac{5}{8}\delta^2\kappa. \tag{6.12}$$

This is essentially the same result summarized by (6.21) in the analysis of Fraenkel, who estimated the ratio of core centroid radius to stagnation point radius as

$$\frac{\rho_{centroid}}{\rho_{stagnation}} = 1 - \tfrac{5}{8}\epsilon'^2 + \ldots, \tag{6.13}$$

where ϵ' denotes the core-to-radius ratio of the slender ring.

Additional remarks

The above discussion immediately enables us to highlight several key features regarding both the asymptotic theory and the resulting thin-tube corrections.

(i) The successful comparison with asymptotic theories for slender rings underscores the fact that our asymptotic treatment of the vorticity transport equation is not limited by any assumptions regarding the shape of the filament reference line or regarding the form of the imposed perturbations. In addition, since the thin-tube model corrections derived on the basis of the analysis are of a local nature, these corrections immediately generalize to any slender vortex filament, irrespective of its background geometry or of imposed perturbations. The only requirement that must be satisfied is that the vortex filament be in fact slender, i.e. the core radius is significantly smaller than the radius of curvature.

(ii) An immediate consequence of the above statement, and of the analyses of §4, is that the asymptotic corrections derived here yield consistent thin-tube models. By consistent, we mean that (*a*) the predicted propagation velocity is consistent with a solution to the vorticity transport equation under the given assumptions regarding the

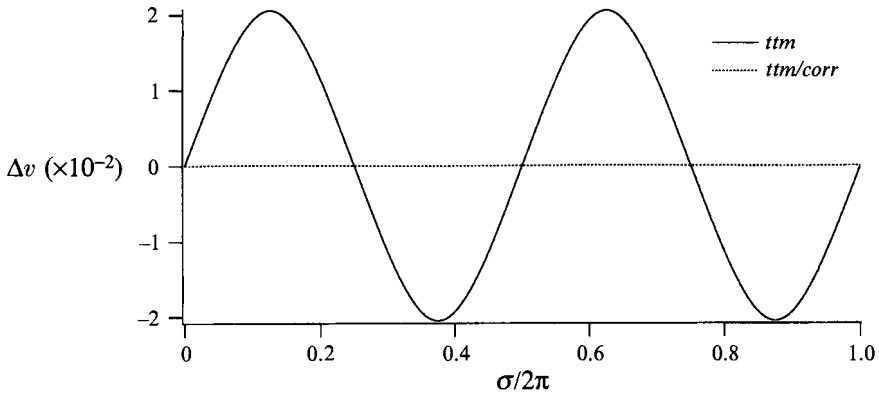

FIGURE 16. Comparison of static velocity predictions for the plane curve initial data from (5.4) using the third-order Gaussian and the sech^2 ($\bar{r}^3$)-core smoothing functions for both the standard (solid line) and the improved (dotted line) thin tube models.

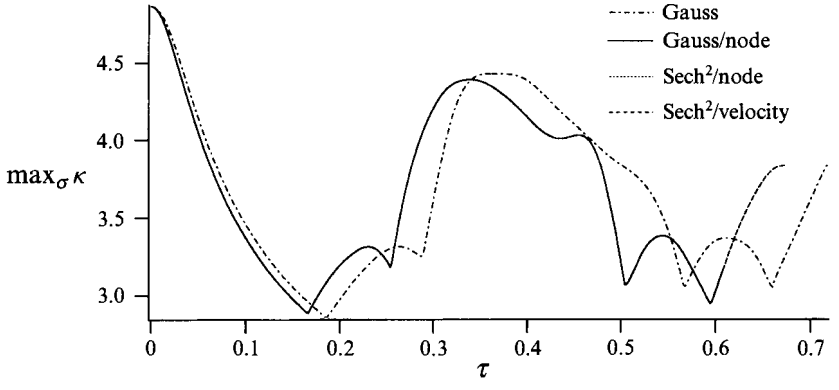

FIGURE 17. Comparison of time histories of the maximum curvature in the computational domain for thin-tube model predictions based on different correction methods.

relevant evolution timescales for the filament, and (*b*) the computational predictions are independent of the desingularization of the line Biot–Savart integral.

The latter assertion is examined in figures 16 and 17, in which we analyse velocity predictions obtained using different core smoothing functions. In figure 16, we plot the static velocity predictions for the plane sinusoidal displacements from (5.4) using the third-order Gaussian and sech^2 ($\bar{r}^3$) core functions from (5.3) for both the standard and improved thin-tube models. The graph shows the velocity differences ($v^{ttm}_{gauss} - v^{ttm}_{sech^2}$) for the standard model (solid line) and for the corrected scheme (dotted line). While the relative deviation for the standard model is of the order of 10^{-2}, the deviations for the corrected schemes are about three orders of magnitude smaller. In the graph this curve appears just as a zero line. The differences between the corrected scheme predictions from equal core functions but different correction approaches are another order of magnitude smaller (not shown). (We also omit displaying several experiments conducted at much higher perturbation amplitudes which also show that the agreement between different correction strategies and different core smoothing functions persists for perturbations well outside the K & M perturbation regime.)

Figure 17 shows the time history of the maximum curvature for a computation with the plane curve distortions from figure 16 as initial data. The two curves for the

corrected thin-tube schemes with Gaussian and $\mathrm{sech}^2(\bar{r}^3)$ core functions coincide within the graphical resolution. The relative deviations are less than 5×10^{-4}. For completeness we have included the curve obtained with the standard model in order to exhibit the considerable modification introduced by the asymptotic corrections and to emphasize that all corrections yield the same modification for all practical purposes.

(iii) It is interesting to note that both the local core structure (and the asymptotic corrections) are completely characterized by the expansion parameter ϵ, which reflects the impact of both the core size and the prevailing vorticity distribution. In this work, we have focused on large-Reynolds-number vortices $\Gamma/\nu = O(\delta^{-1/2})$, and filament geometries for which ϵ is effectively constant on the relevant length- and timescales. In general, ϵ depends on space and time and its evolution can be described only by solving a suitable system of vortex core evolution equations, coupled with the filament dynamics, see e.g. Callegari & Ting (1978) or Ting & Klein (1991). Such general situations will be considered in future work (Klein *et al.* 1994), and compared with various *ad hoc* approximations for the evolution of the vortex core diameter, for example on a conservation-of-volume constraint.

(iv) It is also interesting to note that self-induced velocity errors associated with desingularized line Biot–Savart integrals have been known for quite some time. A well-known example arises in the 'cut-off' formula proposed by Rosenhead (1930):

$$\boldsymbol{u}(\boldsymbol{X}) = \frac{\Gamma}{4\pi}\oint_L \frac{\boldsymbol{t}\times(\boldsymbol{X}-\boldsymbol{X}')}{[(\boldsymbol{X}-\boldsymbol{X}')^2+\mu^2\delta^2]}\,\mathrm{d}\sigma', \tag{6.14}$$

where the parameter $\mu = 1$ is typically associated with uniform cores of radius δ. The inability of this desingularization form to predict the self-induced velocity of thin rings of constant vorticity has been discussed by Saffman (1992), although until now the origin of such errors has remained mysterious.

We emphasize that the asymptotic analyses presented in §§2–3 can be used to derive, elegantly, appropriate corrections for the Rosenhead desingularization, and to justify *ad hoc* parameter selection in cut-off approximations. Although within immediate reach, we do not pursue these objectives here. The primary reason for avoiding the Rosenhead cut-off is that, unlike the adopted desingularization, explicit velocity–vorticity relations are not available, so that the construction of velocity corrections must rely on several cumbersome numerical integration and differentiation procedures. Meanwhile, the cut-off approach is avoided for computational reasons. Numerical implementation of this approach requires an arclength representation of the filament reference line. In conjunction with a Lagrangian approach which is based on direct evaluation of the line Biot–Savart integral, the latter requirement leads to an unnecessarily clumsy computational algorithm.

6.2. *Computational perspectives*

Numerical implementation of Lagrangian thin-tube models is far from trivial. Here we provide a brief discussion – solely from a computational perspective – of the origin of numerical difficulties and of means to overcome them.

Resolution requirements

In numerically modelling the evolution of slender vortices using the thin-tube approach, one is faced with severe spatial resolution requirements. These derive from the vortex element method whose convergence requires, in particular, that neighbouring vortex elements maintain overlapping cores (Beale & Majda 1982*a*, *b*; Beale 1986; Greengard 1986; Ghoniem *et al.* 1988; Knio & Ghoniem 1991). From a practical

point of view, these resolution requirements result in one major computational disadvantage: the simulation must generally carry a very large number of nodes in order to ensure a proper representation of the *local* core structure, i.e. one that is effectively independent of the numerical discretization. Since in the present case, the local core dynamics are quasi-steady and can be accounted for through a time-independent core structure coefficient, the adopted discretization is essentially 'over-refined'. By this, we mean that the number of degrees of freedom used by the thin-tube model is much larger than that required to model the relevant dynamics, which occur at lengthscales much larger than the local core structure. Ideally, one would like to carry a number of elements just large enough to ensure that the slender filament geometry is well represented, and that the numerical evaluation of the *non-local* part of the line Biot–Savart integral is converged. In the present versions of the thin-tube model, these requirements are simply not sufficient. Consequently, it is not surprising that the number of vortex elements needed to ensure spatial convergence in the present thin-tube simulations ($N \sim 1000$) is roughly one order of magnitude larger than the number of modes needed for spatial convergence of the corresponding slender core asymptotic simulations ($N \sim 100$). Though a suitable analytical representation of the local core dynamics, the asymptotics have in fact achieved a significant advantage over the thin-tube model. This advantage is further highlighted by the fact that a single time step in the thin-tube model requires $O(N^2)$ operations, while only $O(N \log N)$ operations are needed in the asymptotics simulations.

While several approaches aimed at overcoming the above disadvantage may be formulated (these are inspired by the asymptotics), we have opted not to pursue such options in the present work. One primary reason is that maintaining overlapping cores guarantees the convergence of thin-tube simulations. Below, we re-examine this statement in view of results obtained using the thin-tube model with spectral representation of the filament geometry as given in §4.4.

Spectral representation of the filament geometry

In developing the improved thin-tube schemes we have not only implemented the asymptotic corrections mentioned in §4, but we have also introduced an important improvement of the numerical discretization that yields rapid convergence of the results with increasing node number. This modification consists of a spectral representation of the curve geometry, which is used both in the evaluation of arclength derivatives and the line Biot–Savart integral. The implementation is based on a Fourier representation of the node locations, which is self-suggesting since periodic perturbations are considered. The modification is also motivated by a desire to obtain smooth and accurate description of arclength derivatives, particularly for the first two versions of the corrected schemes, because the corrections rely on explicit computations of local curvatures and of the filament attached basis vectors $(\boldsymbol{t}, \boldsymbol{n}, \boldsymbol{b})$.

In the light of detailed numerical experimentation, we have established that the spectral code yields much more rapid convergence of the results as long as we consider long-wave data. This is the case, because any variation of the filament geometry on lengthscales comparable to the core diameter means that we have left the regime of validity of the general slenderness assumption, which is the basis of all the asymptotic as well as numerical predictions in this paper. We emphasize that the improved convergence of the method is not limited to the corrected thin-tube models, but also extends to the standard scheme since the numerical evaluation of the line Biot–Savart integral also takes advantage of the spectral representation of the filament geometry.

These features are demonstrated in figure 18, which shows velocity differences for the

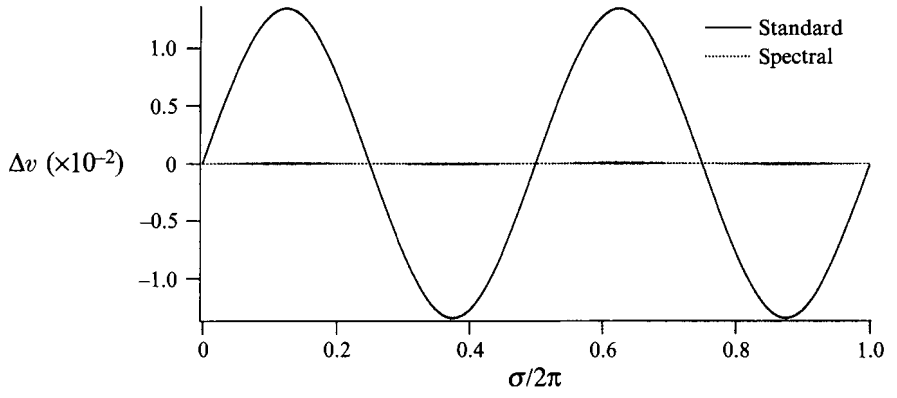

FIGURE 18. Convergence study for the thin-tube models with standard physical space and spectral geometry representation based on static velocity predictions for the plane curve initial data used in figure 16 using 2048 and 1024 nodes.

static case similar to figure 16. We display velocity differences between numerical predictions based on 1024 and 2048 elements. The solid line has been generated with the standard physical space geometry representation of Knio & Ghoniem (1990). The resolution refinement by a factor of two still induces relative changes of the predicted node velocities of the order 10^{-2}. The dotted line shows the effect of the same refinement on the spectral code predictions. We find that these results are practically converged with relative changes being smaller than 2×10^{-5}.

Stiffness of the system

The resolution requirements of the thin tube models are compounded by numerical integration difficulties associated with the stiffness of the system of evolution equations for the Lagrangian coordinates of the elements. Since most of these problems are 'generic' of a large number of Lagrangian conservation law problems, only a brief summary of relevant items is provided.

(i) The stiffness of the system of governing equations necessitates an excessively small integration time step. In the thin-tube computations, we have adopted a variable-step second-order predictor-corrector scheme, and have imposed a time-step constraint of the form $\Delta t = \vartheta \delta^{ttm}/|\boldsymbol{u}_{max}|$, $\vartheta < 1$. Through detailed numerical experimentation (not shown), small values $\vartheta \leqslant 0.02$ are found necessary to ensure a convergent time integration; we have thus used $\vartheta = 0.02$ in all thin-tube calculations discussed above. Thus, the maximum displacement of a node during a single time step is only a small fraction of the vortex core size.

It should be noted that the above time-step restriction requires, in particular, that the numerical integration resolves timescales that are much smaller than the vortex core turnover timescale. Since the core dynamics are assumed to be quasi-steady, and since the filament geometry evolves at significantly larger timescales than those characterizing the rapidly rotating slender core, the present restrictions are extremely severe. This severity can be further highlighted by comparison with asymptotic simulations, which enable simple explicit split-step semi-spectral implementation with timesteps scaling with the actual characteristic evolution time of the filament to be employed (Klein & Majda 1991*b*). For a typical computational experiment from §5 the ratio of timesteps $\Delta t^{ttm}/\Delta t^{K\&M} \approx \frac{1}{10}$.

It should also be noted that the variable-step algorithm incorporated in the computations may not constitute the optimal approach for tackling the stiffness of the

system. However, owing to the simplicity of the adopted approach, we did not explore more sophisticated time-integration algorithms.

(ii) The stiffness of the system of governing equations is compounded by the susceptibility of the computations to round-off errors. The origin of this latter problem appears to be due to two related issues. The first is associated with the resolution requirements discussed above, which necessitate a very large number of spatial modes. The second is due to the evaluation of the filament velocity which is based on direct summation over the fields of all the elements. Since neighbouring elements induce large $O(\delta^{-2})$ velocities on each other, the calculation relies on the cancellation of $O(\delta^{-2})$ velocity components in order to estimate an $O(\ln(1/\delta))$ filament velocity. As discussed below, the susceptibility of the computations to round-off errors complicates the implementation of the spectral algorithm to unsteady simulations, and motivates further refinement of the numerical scheme.

(iii) We finally note that the 'symptoms' of time-integration problems are easy to detect. Through detailed numerical experimentation (not shown), two distinct manifestations of time-integration problems can be observed. The first mild symptom, which consists of the appearance of high-frequency numerical noise in the computed solution, occurs once the integration time step slightly exceeds a threshold value. The selection of even larger time steps leads to a catastrophic breakdown of the computations. This breakdown occurs as a result of an unphysical overturning wave which leads to the local collapse of the filament on itself. However, since a brute-force systematic time-step reduction approach easily cures these difficulties, further discussion of these numerical phenomena is omitted.

Nonlinear filtering

The improved properties of the spectral algorithm established in static experiments do not immediately extend to time-dependent calculations. Despite the fact that the spectral representation yields very accurate velocity predictions, a straightforward implementation of these techniques and of the velocity corrections is found to have a destabilizing impact on the computations. This destabilization is weakly affected by time discretization errors; on the other hand, high-frequency round-off errors have a strong negative impact on this phenomenon. Thus, decreasing already minute integration errors through further reduction of the time step does not completely cure the problem. This motivates the incorporation of a nonlinear filtering procedure in order to remove high-frequency noise.

The adopted filtering procedure developed here is an extension of the two-dimensional version proposed by Krasny (1983). The algorithm acts on the Fourier components of the curve geometry by identifying and eliminating, at every integration time step, all modes having amplitude below a prescribed threshold. Reliable and robust results have been obtained with an elimination threshold of 10^{-12}. We emphasize that this small value is at the limit of resolution of a single-precision representation on a CRAY C90 where thin-tube computations have been carried out. Thus, no sizable numerical damping is introduced; rather, high-frequency noise is eliminated once it is generated.

It is finally emphasized that, for all the cases considered here, the incorporation of the filtering algorithm into the original straight-segment representation scheme is not necessary. This is not surprising since in the latter approach, spectral collocation differentiation of high-frequency noise is not performed. Furthermore, through favourable comparison of the results of well-resolved straight segment and spectral representation simulations, we note that the nonlinear filtering procedure used in this

work does not prevent the generation of higher frequency modes through relevant nonlinear phenomena, but prevents their introduction due to numerical errors. This observation is in agreement with Krasny's (1983) experience gained through the application of similar schemes to the study of singularity formation in two-dimensional vortex sheets.

The authors thank Professors Lu Ting and Andrew J. Majda for their encouragement and for stimulating discussions during the initial stages of this research. Furthermore they are indebted to the Pittsburgh Supercomputing Center, where all of the thin-tube model computations were performed.

Appendix A. Periodic boundary conditions for the thin-tube model

Another distinctive feature of the present thin-tube model computations concerns the treatment of periodic boundary conditions. When L-periodic perturbations of a thin filament are considered, the computational domain is defined by a single channel of height L along the periodicity direction and it is unbounded in the remaining two. In order to enforce the periodicity of the velocity field, the image system of the vortex elements outside the computational domain must be accounted for when the formula in (4.5) is evaluated. To this end, we assume the periodicity direction to coincide with the x-direction of a right-handed coordinate system (x, y, z) with basis vectors $(\boldsymbol{e}_1, \boldsymbol{e}_2, \boldsymbol{e}_3)$, and consider the velocity component, $\boldsymbol{u}_o$, induced by a single vortex element of length $\delta\boldsymbol{\chi} = (\Delta x, \Delta y, \Delta z)$ centred at $\boldsymbol{\chi}^c = (x_o, y_o, z_o)$. We have

$$\boldsymbol{u}_o(\boldsymbol{x}) = \frac{\Gamma}{4\pi} \sum_{k=0}^{\pm\infty} P(\boldsymbol{\chi}^c - \boldsymbol{x}, \delta\boldsymbol{\chi}, k)\, Q(\boldsymbol{\chi}^c - \boldsymbol{x}, k), \tag{A 1}$$

where

$$P(\boldsymbol{x}, \delta\boldsymbol{\chi}, k) = \frac{(\boldsymbol{x} + kL\boldsymbol{e}_1) \times \delta\boldsymbol{\chi}}{|\boldsymbol{x} + kL\boldsymbol{e}_1|^3} \tag{A 2}$$

and

$$Q(\boldsymbol{x}, k) = \kappa_\delta(\boldsymbol{x} + kL\boldsymbol{e}_1). \tag{A 3}$$

In (A 1), the contribution of the image system of the element is handled exactly. Unfortunately, the infinite sum appearing in this expression does not admit a simple closed form expression as was shown by Knio & Ghoniem (1991, 1992). To overcome this difficulty, we first decompose the sum into two components, $\boldsymbol{u}_1$ and $\boldsymbol{u}_2$, which respectively correspond to the contributions of the element itself and of its image system. The first component is computed directly,

$$\boldsymbol{u}_1(\boldsymbol{x}) = \frac{\Gamma}{4\pi} \frac{(\boldsymbol{\chi}^c - \boldsymbol{x}) \times \delta\boldsymbol{\chi}}{|\boldsymbol{\chi}^c - \boldsymbol{x}|^3} \kappa_\delta(\boldsymbol{\chi}^c - \boldsymbol{x}), \tag{A 4}$$

while the second is first approximated as

$$\boldsymbol{u}_2(\boldsymbol{x}) \approx \frac{\Gamma}{4\pi} \sum_{k=\pm 1}^{+\infty} P(\boldsymbol{\chi}^c - \boldsymbol{x}, \delta\boldsymbol{\chi}, k), \tag{A 5}$$

i.e. the effect of the core smoothing function is neglected from the contribution of the image system since we assume $L \gg \delta$. After straightforward manipulations, (A 5) is rewritten as

$$\boldsymbol{u}_2(\boldsymbol{x}) \approx \frac{\Gamma}{4\pi} [F(x_o - x, y_o - y, z_o - z)\{(\boldsymbol{\chi}^c - \boldsymbol{x}) \times \delta\boldsymbol{\chi}\} - \Delta z G(x_o - x, y_o - y, z_o - z)\, \boldsymbol{e}_2 + \Delta y G(x_o - x, y_o - y, z_o - z)\, \boldsymbol{e}_3], \tag{A 6}$$

where

$$F(x_o-x, y_o-y, z_o-z) = \sum_{k=\pm 1}^{\pm\infty} \frac{1}{[(x_o+kL-x)^2+(y_o-y)^2+(z_o-z)^2]^{3/2}}, \tag{A 7}$$

$$G(x_o-x, y_o-y, z_o-z) = \sum_{k=\pm 1}^{\pm\infty} \frac{kL}{[(x_o+kL-x)^2+(y_o-y)^2+(z_o-z)^2]^{3/2}}. \tag{A 8}$$

In a preprocessing step, the functions F and G are evaluated numerically by truncating the summation at a large index. The computed values are stored in two-dimensional arrays which are interpolated during the computations. The truncation of the summation is done such that the contributions of the 500 images closest to the computational domain in each direction are accounted for. The evaluation of the sums is performed on a fine grid in order to minimize interpolation errors. This necessitates a somewhat large storage requirement, which is optimized by only tabulating half the needed values and exploiting the following relationships:

$$F(x_o-x, y_o-y, z_o-z) = F(|x_o-x|, |y_o-y|, |z_o-z|), \tag{A 9}$$

$$G(x_o-x, y_o-y, z_o-z) = \operatorname{sign}(x_o-x)\, G(|x_o-x|, |y_o-y|, |z_o-z|). \tag{A 10}$$

The technique detailed above yields estimates of the velocity component induced by the entire image system of a single element. To obtain the total velocity field, summation over the image systems of all the elements must be performed. In doing so, the vortex interaction algorithm ensures that the assumption that the core smoothing function acts on the nearest vortex element is satisfied by using the following technique. In order to estimate the velocity field at a point z inside the computational domain, the algorithm first performs a translation of the entire domain along the periodicity direction, $x \to x' = x+d$, so that z' coincides with the centre of the original domain. This coordinate translation is also applied to the Lagrangian locations of the vortex elements. Based on the translated locations, the algorithm identifies exactly the members of all image systems which lie within the original computational domain. The locations of these elements are then used in the summation described above. This procedure enables us to enforce periodicity boundary conditions accurately, since exact expressions are tabulated almost to within machine accuracy and interpolated on fine grids, and efficiently, since the required computational overhead represents a small fraction of the effort needed to compute vortex interactions in an unbounded domain.

Appendix B. Space–time rescaling for comparison of theoretical and numerical predictions

A typical radius of curvature R of the filament reference line and its cirulation Γ define the reference time

$$t_{ref} = 4\pi R^2/\Gamma \tag{B 1}$$

which is used as characteristic timescale and normalizing quantity in thin-tube model computations. Meanwhile, the reference time used by the K&M theory, which characterizes the oscillations of $O(\epsilon^2)$ perturbations away from a straight line is, according to (2.9),

$$t_{ref}^{K\&M} = \epsilon^4 t_{ref} \tag{B 2}$$

with ϵ defined in (1.12).

The plane curve initial data from (5.4) and (5.9*a*, *b*) are periodic with period 2π in the s-coordinate, which is a linear coordinate on the unperturbed straight line. This

periodicity structure is suitable for the thin-tube computations, but it is not convenient for the numerical solution of the filament equation. The relevant spatial coordinate in (2.12) is an arclength variable and the semi-spectral algorithm for the solution frequently uses fast Fourier transforms and the exact solution of the linear part of (2.12) in Fourier space. The code we use is designed for 2π-periodic data. In order to avoid implementing cumbersome modifications to the code, we employ the following scale transformations which map the filament function into a 2π-periodic image that also solves (2.12), but with a rescaled value of ϵ^2.

Thus, let

$$\gamma = \mathscr{A}/2\pi \tag{B 3}$$

be the ratio of the arclength $\mathscr{A}$ within a period of the initial filament reference line and the desired period length 2π after rescaling. Now, if $\psi(\sigma, \tau)$ solves (2.12), then

$$\psi^*(\sigma^*, \tau^*) = \gamma\psi(\sigma, \tau) \tag{B 4}$$

with

$$\sigma^* = \sigma/\gamma \quad \text{and} \quad \tau^* = (1+\epsilon^2 \ln\gamma)\,\tau/\gamma^2 \tag{B 5}$$

also solves the filament equation, but with the rescaled value of the coupling parameter

$$\epsilon^{*2} = \epsilon^2/(1+\epsilon^2 \ln\gamma). \tag{B 6}$$

A tedious but straightforward calculation shows that this rescaling of the coupling parameter occurs because of the Heaviside step function in the definition of the I-operator in (2.10).

REFERENCES

Arms, R. J. & Hama, F. R. 1965 *Phys. Fluids* **8**, 533.

Batchelor, G. K. 1967 *An Introduction to Fluid Dynamics*. Cambridge University Press.

Beale, J. T. 1986 *Math. Comput.* **46**, 401.

Beale, J. T. & Majda, A. 1982*a* *Math. Comput.* **39**, 1.

Beale, J. T. & Majda, A. 1982*b* *Math. Comput.* **39**, 29.

Beale, J. T. & Majda, A. 1985 *J. Comput. Phys.* **58**, 188.

Callegari, A. J. & Ting, L. 1978 *SIAM J. Appl. Maths.* **35**, 148.

Chorin, A. J. 1980 *SIAM Sci. Statist. Comput.* **1**, 1.

Chorin, A. J. 1982 *Commun. Math. Phys.* **83**, 517.

Chorin, A. J. & Akao, J. 1991 *Physica* D **52**, 403.

Crow, S. C. 1970 *AIAA J.* **8**, 2172.

Fraenkel, L. E. 1972 *J. Fluid Mech.* **51**, 119.

Ghoniem, A. F., Heidarinejad, G. & Krishnan, A. 1988 *J. Comput. Phys.* **79**, 135.

Greengard, C. 1986 *Math. Comput.* **47**, 387.

Hasimoto, H. 1972 *J. Fluid Mech.* **51**, 477.

Klein, R. 1994 *Zur Dynamik schlanker Wirbel. einger. zur Habilitation.* RWTH Aachen.

Klein, R. & Majda, A. 1991*a* *Physica* D **49**, 323.

Klein, R. & Majda, A. 1991*b* *Physica* D **53**, 267.

Klein, R. & Majda, A. 1993 *Phys. Fluids* A **5**, 369.

Klein, R., Majda, A. & McLaughlin, R. M. 1992 *Phys. Fluids* A **4**, 2271.

Klein, R. & Ting, L. 1992 *Appl. Math. Lett.* **5**, 99–103.

Klein, R., Ting, L. & Knio, O. M. 1994 Accurate numerical computation of stretched, high-Reynolds-number, slender vortices in three space dimensions. In preparation for *3rd. Intl Congress on Industrial and Applied Maths, Hamburg, Germany, June 1995.*

Knio, O. M. & Ghoniem, A. F. 1990 *J. Comput. Phys.* **86**, 75.

Knio, O. M. & Ghoniem, A. F. 1991 *J. Comput. Phys.* **97**, 172.

KNIO, O. M. & GHONIEM, A. F. 1992 *J. Fluid Mech.* **243**, 353.

KRASNY, R. 1983 *J. Fluid Mech.* **167**, 65.

LEONARD, A. 1985 *Ann. Rev. Fluid Mech.* **17**, 525.

LIU, C. H., TAVANTSIS, J. & TING, L. 1986 *AIAA J.* **24**, 1290.

PUMIR, A. & SIGGIA, E. 1990 *Phys. Fluids* A **2**, 220.

ROSENHEAD, L. 1930 *Proc. R. Soc. Lond.* A **127**, 590.

SAFFMAN, P. G. 1992 *Vortex Dynamics*. Cambridge University Press.

THOMSON, J. J. 1883 *A Treatise on the Motion of Vortex Rings*. Macmillan.

TING, L. 1971 In *Aircraft Wake Turbulence and its Detection* (ed. J. H. Olsen, A. Goldburg & M. Rogers), pp. 11–39. Plenum.

TING, L. & KLEIN, R. 1991 *Viscous Vortical Flows*, Lecture Notes in Physics, vol. **374**. Springer.

VITTING, T. 1991 *Struktur von Flugzeugrandwirbeln und Massnahmen zur Wirbelabschwaechung*. VDI Verlag Duesseldorf, Germany.

WIDNALL, S. 1975 *Ann. Rev. Fluid Mech.* **7**, 141–165.